

Jonathan Z. Sun

Contents

Spin-Polarized Transport Across Interfaces and Spin Torque: An Overview	1341
Basic Concepts in Noncollinear Spin-Polarized Transport	1341
Metal-to-Metal Interface and Spin Valves	1343
Tunnel Barrier and Magnetic Tunnel Junctions	1346
Origins of Spin Torque	1348
The Macrospin as a Model System	1348
Torque and Dynamics of a Macrospin	1348
A Review of Spin-Containing Quantities and Spin Transport	1349
Origins of Spin Torque	1352
Modified LLG Equation with a Spin-Torque Term	1355
Spin-Torque-Induced Magnetodynamics	1356
Time Scales, Length Scales, and Constitutive Relationship for	
Spin-Torque Dynamics in Continuous Medium	1356
Zero-Temperature Macrospin Dynamics	1359
Finite-Temperature Macrospin Dynamics	1361
Switching Speed and Dynamics of a Macrospin Under Spin Torque	1363
Exchange Stiffness, Internal Degrees of Freedoms, and Magnons	1368
Experiments	1370
Spin-Torque-Induced Magnetic Excitation and Switching	1370
Spin Torque in Magnetic Tunnel Junctions	1371
Applications	1372
Spin-Torque Switchable Magnetic Tunnel Junction as Memory Devices	1373
Nonlocal Spin-Current and Three-Terminal Spin-Torque Devices	1377
Open Questions and Future Challenges for Spin-Torque Science and Technologies	1380
References	1382

J.Z. Sun (✉)
IBM Research, Yorktown Heights, NY, USA
e-mail: jonsun@us.ibm.com

Abstract

Spin torque refers to the exchange of spin angular momentum between a transport spin current carried by electrons and a ferromagnet. The macroscopic manifestation of this angular momentum exchange is a torque exerted on the ferromagnet by the presence of the spin current. The spin current is often accompanied by a net charge-current transport, although this is not always necessary. There are two types of torque commonly associated with such interactions, one is exchange-like and the other energy nonconserving. These two types of torques have different vectorial relationship with the electron spin polarization and the magnet's moment. The exchange-like torque is in the direction perpendicular to the plane formed by the magnet moment and the spin polarization and is therefore often called the "perpendicular torque." The energy-nonconserving torque lies in the plane, hence the name the "in-plane torque." The perpendicular torque has been known for many decades, as it gives rise to exchange-like coupling between ferromagnetic thin films across a spacer layer of either a nonmagnetic metal or a tunnel barrier. A detailed understanding of the in-plane spin torque has emerged more recently. The in-plane spin torque is associated mainly with nonequilibrium and noncollinear transport of spin current across interfaces between nonmagnetic and ferromagnetic materials. It originates from the dephasing of an electron's spin precession as it enters or leaves a ferromagnet–nonmagnetic interface. The in-plane spin torque gives rise to new dynamic behaviors of the ferromagnet that is the subject of many interesting investigations and with potential for applications. Its physical origin and implications are the main subjects of this review.

List of Abbreviations

AFM	Antiferromagnetic
AP-P	Antiparallel to parallel
CPP	Current Perpendicular to plane
FL	Free layer
FM	Ferromagnetic
GMR	Giant magnetoresistance
I	Insulator or tunnel barrier
IL	Injection layer
IMA	In-plane magnetic anisotropy
MOS-FET	Metal oxide semiconductor field-effect transistor
MTJ	Magnetic tunnel junction
N	Nonmagnetic metal
P-AP	Parallel to antiparallel
PMA	Perpendicular magnetic anisotropy
RL	Reference layer
SAF	Synthetic antiferromagnet
SEM	Scanning electron microscopy

STT	Spin-transfer torque
SV	Spin valve
TEM	Transmission electron microscopy
TMR	Tunnel magnetoresistance

Spin-Polarized Transport Across Interfaces and Spin Torque: An Overview

Spin-dependent transport across interfaces controls many aspects of magnetoresistance in inhomogeneous ferromagnetic/nonmagnetic transition metal conductor systems. Over the years a “two-current” transport model has been developed to describe such transport process. The concept originates from the approximate treatment of transition metal transport scattering process by noticing a spin-flip scattering lifetime generally longer than that of the momentum-space scattering time. With this assumption each spin eigenstate can be treated as effectively decoupled from the other in noninteracting electron band-structure-based transport models. This spin-separated two-current approach was first developed for analyzing transport physics in homogeneous ferromagnetic transition metal conductors such as Fe and Ni [1, 2]. It has since been successfully expanded to inhomogeneous conductor systems containing either ferromagnetic metal-to-nonmagnetic metal interfaces or to ferromagnetic systems containing sharp magnetic domain walls. Among such the most quantitatively treatable has been the spin-dependent transport across interfaces between ferromagnetic and nonmagnetic transition metals in the so-called current-perpendicular-to-plane (CPP) spin valves (SV) [3–5].

On a slightly different front, a similar two-channel conduction concept has been employed to account for the spin-dependent tunneling of electrons from one ferromagnetic metal into another, separated by a tunnel barrier, whose barrier height for each spin channel may or may not be the same [6–9]. This concept was developed to describe the so-called tunnel magnetoresistance (TMR) phenomenon, in which case the tunnel conductance of a ferromagnet–insulator–ferromagnet (FM/IFM) tunnel junction varies depending on the relative orientation of the ferromagnet’s moment direction.

Basic Concepts in Noncollinear Spin-Polarized Transport

Most of these earlier transport descriptions discussed above (except Slonczewski’s [8]) assume that for the entire system of interest, the carriers have two well-defined spin eigenstates – that of spin-up and that of spin-down for a spin-1/2 carrier such as electrons, with “up” and “down” defined by the moment direction of the ferromagnet in question. Further one assumes that there is virtually no interaction or correlation between carriers in these two spin states, other than local charge neutrality [10]. This second assumption is important because it is equivalent to saying that the

ferromagnets in this system would have to have a single uniquely defined direction for its macroscopic order parameter, i.e., their magnetizations are collinear.

The two-channel conduction picture was developed to sufficient quantitative details to account for the observations of, among other things, the so-called giant magnetoresistance or GMR effect in thin metal film stacks with CPP transport, in which case the different layers of ferromagnets are separated by a thin layer of nonmagnetic metal in between. A comprehensive discussion on the two-channel model for CPP GMR can be found in, for example, Ref. [3]. A detailed review of the CPP- GMR materials and properties is covered in ► [Chap. 4, “CPP-GMR: Materials and Properties”](#), Part II, Volume 1.

Theory for magnetotransport involving noncollinear magnetic moment arrangements was developed to compare with the angular dependence of the GMR [11, 12] as well as TMR [8, 13]. The quantitative understanding of noncollinear spin transport is key to understanding the spin-torque phenomenon. Without collinear alignment, the effect of coherence between the different spin eigenstates becomes important. Generally this involves coherent decomposition of one set of spin eigenstates into that of another. For spin-1/2 fermion states such as with electrons, it can be conveniently described by a 2×2 Pauli matrix spinor formulation.

For spin-dependent transport studies, it is important to keep track of this eigenstate decomposition as the relevant transport wave functions propagate and reflect among various media and interfaces involving noncollinear ferromagnet elements. This is nontrivial, as a carrier now would in principle need to be treated with the full complex wave function including spin space, and these are generally not diagonalized in any fixed spin-space direction. With noncollinear spin orientation, a carrier upon entering a ferromagnet from an interface would necessarily be decomposed into a set of coherent spin eigenstates at the point of entry. This is if the situation is such that an approximately localized wave function (a wave packet with relatively narrow momentum spread to allow definition of an average momentum \mathbf{k}_s , but at the same time with sufficiently narrow spatial spread to allow definition of a spatial location) can be used to describe the propagation while maintaining real-space boundary conditions at the same time. It is in this regime a quasi-classical particle picture can be useful to imagine the transport as being carried by a particle-like electron. Here the subscript in \mathbf{k}_s , as $s = \pm$ corresponds to the up- or down-spin states as defined by the ferromagnet’s moment near the interface. In its semiclassical representation, the electron entering the ferromagnet is seen as precessing around the exchange field as it propagates along.

In a ferromagnet with strong exchange splitting, this decomposition is simplified. Because of the large exchange split, the wave vectors \mathbf{k}_\pm are very different at the Fermi level. This brings wave functions with rapid spatial oscillation in its spin-state amplitudes along the direction of propagation in real space, with a characteristic length of the order $1/|\mathbf{k}_+ - \mathbf{k}_-|$ inside the ferromagnet. Rapid spatial decoherence follows, especially when this \mathbf{k}_s vector has any significant spread in direction for states involved in the transport, which is the case for many interfaces between different transition metals for which a large region of the Fermi surfaces from both metals is involved [11, 14, 15]. In such systems, such as $\parallel\text{Co/Cu/Co}\parallel$ CPP

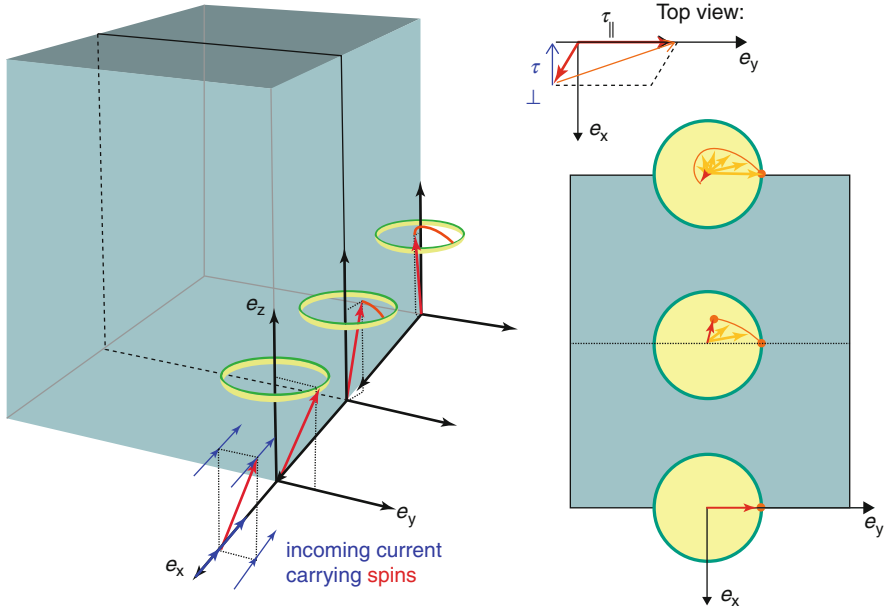


Fig. 1 The precession- and position-dependent decoherence of carrier spins upon entering a ferromagnet. The red arrow represents the average electron spin at the given position. e_z is the direction of the FM's magnetization

structures, it is safe to assume that the spin precession of the carrier electrons entering through (or reflecting from) a nonmagnetic/ferromagnet interface becomes fully incoherent within a very short distance from the interface, on the order of an inverse Fermi wave vector, thus losing its average spin angular momentum in the direction transverse to the magnetization. This process of carrier spin precession and its decoherence is illustrated in Fig. 1.

This rapid decoherence has significant implications for angular momentum conservation. If one examines a spin-current transport across any one such interface, one realizes that the decoherence corresponds to the loss of the transverse component of the spin angular momentum from the carrier current. Since the interaction is between the ferromagnet's collective magnetically ordered state that provides the local exchange and that of the transport carrier spin, angular momentum conservation dictates that the lost transverse component of the carrier spin be represented as a torque on the total magnetic moment of the ferromagnet. This is the origin of the so-called spin-transfer torque (STT) or spin torque for short.

Metal-to-Metal Interface and Spin Valves

In all-metal multilayered CPP structures, an ultrathin (usually on the order of several nanometers) ferromagnet and nonmagnetic metal film stack is the active component.

Such a spin-valve junction, in the form of $\parallel\text{Co/Cu/Co}\parallel$, for example, together with top and bottom metallic leads forms the basic structure. These have been well studied for the past few decades for GMR, with the stack's electrical resistance being influenced by the relative orientation of the two magnetic layers. The reverse of which, namely, an action of the spin-polarized current on the magnetic moment, is a direct consequence of the transverse spin angular momentum transfer due to the decoherence discussed above, giving rise to a spin-transfer torque on the ferromagnet.

The concept of a conduction electron's spin angular momentum acting on a ferromagnet via s-d-like exchange dates back many decades in the context of charge-current-induced domain wall movement [16, 17], in the discussion of a type of "dissipative" exchange coupling across a tunnel barrier in spin-dependent magnetic tunnel junctions [8] and in the ability of a spin-polarized current entering a ferromagnet to cause magnetic rotation and/or instabilities for the magnetic moments near that interface [18]. Quantitative predictions were made about consequences of STT on thin multilayered structures of the type $\parallel\text{FM}/\text{NM}/\text{FM}\parallel$ around 1996 by Slonczewski [14] and Berger [19]. The main predictions are that at sufficiently large current density (of the order 10^7 A/cm²) and with sufficient spin polarization, the STT interaction related to the spin-polarized charge-current transport across NM/FM interface would reduce the apparent damping of the FM layer to negative values, resulting in an effective amplification of spin waves and/or macrospin precession that could lead to a complete reversal of the moment of a nanomagnet in a uniaxial anisotropy potential.

The STT-induced magnetic reversal involves dynamics different from magnetic-field-driven reversal [14, 20, 21]. The STT's action is not to directly counterbalance the torque from either a magnetic field or a uniaxial anisotropy field. Instead, the STT appears as an energy-nonconserving force, similar to damping. The leading-order effect of STT is a modification of the effective damping of the ferromagnet. When the damping coefficient turns negative, an amplification of magnetic precession results which can eventually lead to the reversal of the moment. This new effect of STT-induced magnetic excitation and reversal is illustrated in Fig. 2.

Indications of magnetic excitation by spin-polarized current were reported in point-contact magnetic multilayers [22, 23]. Experimental observations of STT-driven magnetic switching were made in highly spin-polarized magnetic oxide multilayer junctions [20, 24], and in well-defined transition metal pillars of $\parallel\text{Co/Cu/Co}\parallel$ [25]. Figure 3 summarizes the work of Katine et al. [25].

The observation of STT switching experimentally confirmed the basic quantitative understanding of the STT-related transport physics and magnetodynamics. It also demonstrated a simple principle for estimating the amount of current required for switching of a nanomagnet under a uniaxial anisotropy potential [14, 20, 21]. In practical units and in its simplest form, it is

$$I_{c0} = \left(\frac{2e}{\hbar}\right) \left(\frac{\alpha}{\eta}\right) mH_k \quad (1)$$

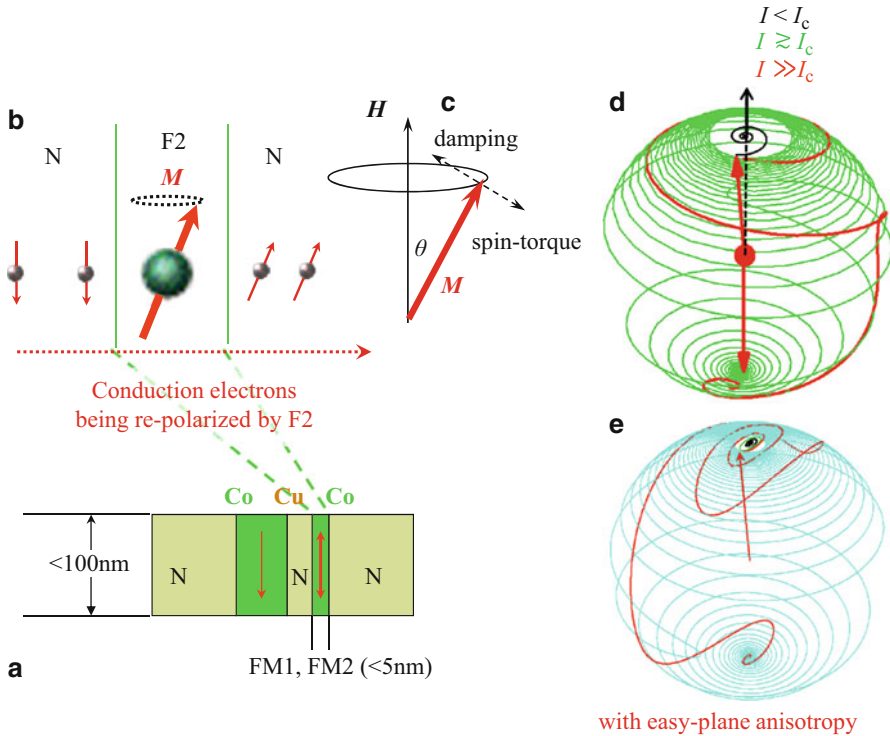


Fig. 2 The transfer of transverse spin angular momentum from conduction electrons to that of a nanomagnet and the effect of the STT torque. (a) A sketch of the basic all-metal spin-valve structure; (b) focus on the thinner FM layer. Electrons with spin-polarization incident onto the N|FM2 interface giving its transverse angular momentum away to FM2, resulting in an effective torque on FM2. (c) The orientation and effect of the torque. (d) The trajectory of the resulting precession of FM2 if in a perfectly uniaxial anisotropy energy potential. When the STT torque exceeds damping torque in the opposite direction, the precession trajectory opens up till it crosses the equator, resulting in a magnetic reversal. (e) A reversal trajectory for a realistic thin-film structure with strong demagnetization-induced easy-plane anisotropy

where I_{c0} is the zero-temperature switching instability threshold, e is the electron charge in Coulomb [C], \hbar is Planck constant in [erg · sec], m is the total magnetic moment in [emu], and H_k the uniaxial anisotropy field in [Oe]. η here is the spin polarization of the charge current passing through the nanomagnet. For a reasonable set of parameters this evaluates to of the order of $1 \mu\text{A}$ per $k_B T$ of energy barrier height for ambient T [20]. This amount of current makes it potentially within reach for electronic device applications such as for solid-state memory.

Switching current requirements aside, the spin-valve type of devices as they were however was generally not suitable for large-scale integrated electronics applications. This is because of a significant mismatch in device impedances with devices used in the established integrated circuit technology. A typical MOS-FET

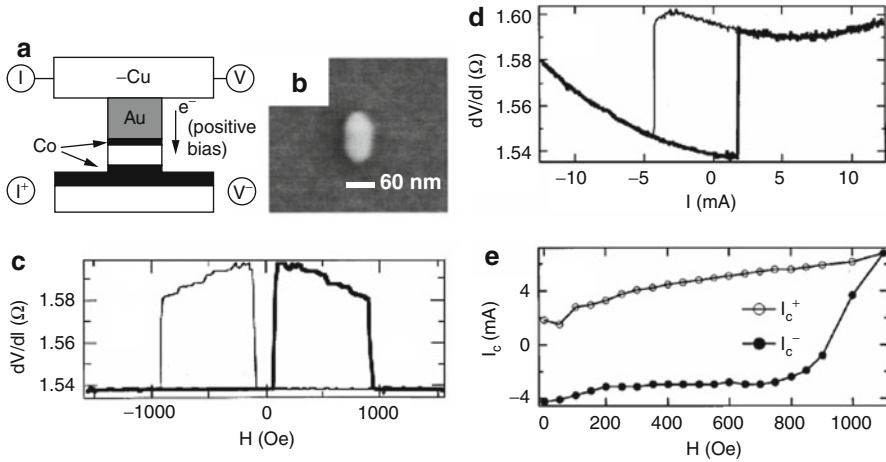


Fig. 3 Demonstration of STT-induced magnetic switching in nanostructured spin valves by Katine et al. [25]. (a) A sketch of the device structure. (b) A top view scanning electron microscopy (SEM) image. (c) The spin-valve junction's GMR versus magnetic-field sweep curve showing the parallel and antiparallel transitions. (d) Same antiparallel-to-parallel (AP-P) and parallel-to-antiparallel (P-AP) transitions driven by current passing through the device. (e) The threshold of switching current as it depends on the bias magnetic field applied along the in-plane easy axis of the GMR device

(for metal-oxide-semiconductor field-effect transistor) device's on-state resistance is of the order of 1 k Ω , whereas a spin-valve device typically has intrinsic resistances on the order of 1 Ω . The small resistance, and relatively small magnetoresistance (on the order of 10 % or less), makes them incompatible with silicon-based integrated circuits of the present day, particularly when it comes to the electrical readout of the magnetic orientation state which has to be done via magnetoresistance signal. Thus, from the applications' point of view, a spin-dependent device similar to the spin valves described so far but with higher impedance is sought for. This makes the discovery of spin-dependent tunnel junction with large TMR an exciting event.

Tunnel Barrier and Magnetic Tunnel Junctions

It has also been known for decades that a ferromagnetic electrode generally would have different density of states at the Fermi level for spin-up and spin-down sub-bands. This difference was quantitatively studied experimentally using a type of ferromagnet-insulator-superconductor tunnel junctions [9]. For tunneling between two ferromagnetic conductors, the tunnel conductance is expected to be dependent on the relative orientations of the two ferromagnetic electrodes [6, 26]. Earlier explorations [7] of such $\parallel\text{FM}_1\parallel\text{IFM}_2\parallel$ tunnel structures in the 1970s and 1980s were done at liquid helium temperature for easier detection of small TMR signals and for quantitative understanding, usually with a small TMR of a few percent.

Experiments first reported in 1995 brought large TMRs for MTJs operating at ambient temperature, enabling their application in consumer electronics industry. Independently Moodera et al. [27] and Miyazaki et al. [28] reported observations of appreciable tunnel magnetoresistances (TMR) over 10 % in thin film $\|\text{CoFe}/\text{Al}_2\text{O}_3/\text{Co}\|$ and $\|\text{Fe}/\text{Al}_2\text{O}_3/\text{Fe}\|$ tunnel junctions at room temperature. Development efforts immediately followed to optimize materials combinations and processing conditions to maximize TMR at low junction-specific resistance, mostly for sensor applications, especially in the magnetic data storage industry.

Another important tunnel barrier material known since at least the early 1980s is MgO [29]. It had been used successfully for superconducting Josephson tunnel junctions with NbN electrodes [30]. MgO prefers to grow crystalline with (100) orientation on many underlayer materials including Fe [31]. First principle band-structure modeling predicted large magnetoresistance of over 1,000 %, for many ferromagnet|MgO|ferromagnet systems such as $\|\text{Fe}(100)/\text{MgO}(100)/\text{Fe}(100)\|$ [32, 33] and $\|\text{Co}(100)/\text{MgO}(100)/\text{Co}(100)\|$ [34] and other similar systems. It was soon experimentally demonstrated that indeed tunnel junctions of MgO barrier have superior properties with large ambient temperature magnetoresistance values around 200 % or higher [35, 36]. At the time of this writing, the best experimentally demonstrated TMR in MgO-based tunnel device stands at a room temperature value of over 600 %, with low-temperature values exceeding 1,000 % at 5 K in CoFeB/MgO/CoFeB tunnel devices [37].

The reason for very large TMR in crystalline MgO-based MTJs is the strong spin polarization for the particular set of electronic states involved in tunneling. Materials such as Fe and Co have only a modest spin polarization for Fermi-surface-averaged density of states. However, for tunneling and especially tunneling in highly (100) oriented crystals interfaced with (100) MgO, only states with very specific momentum \mathbf{k} -vectors are involved, and those states have stronger spin polarization in their density of states. More importantly, these state's decaying characteristics of tunnel probability into the depth of the (100) MgO barrier are very strongly spin dependent, thus causing a very strong spin dependence of the tunnel conductance, giving crystalline tunnel junctions of Fe(001)/MgO(001)/Fe(001) type far larger TMR than similar ferromagnet electrodes using amorphous tunnel barriers such as AlO_x .

Large spin-torque effect in the form of bias-current-induced magnetic switching was also observed in MTJs. The presence of spin torque as a dissipative exchange force across a magnetic tunnel junction interface was predicted earlier [8]. Experimentally, STT-induced magnetic switching was first directly observed in AlO_x -based MTJs [38]. A general framework was developed to quantitatively understand the effect of spin torque in magnetic tunnel junctions [8, 13, 39, 40]. These analyses mostly assumed a low-voltage expansion to the leading order of the tunnel conductance elements. Consequently the tunnel conductances were assumed to be independent of bias. Such a simple model clearly illustrates the difference in accounting for charge-current transport, which relates to TMR, and for spin transport, which relates to spin torques.

Origins of Spin Torque

This section focuses on descriptions of spin angular momentum conservation in various typical CPP transport configurations and the resulting spin torques experienced by the ferromagnets participating in charge and spin-current transport. For this one starts with a somewhat simplified model concept of a nanomagnet, a macrospin.

The Macrospin as a Model System

A model system to examine the principles of spin torque has been illustrated in Fig. 2a, where two ferromagnets, F_1 and F_2 , are separated by a nonmagnetic layer that disrupts the nearest neighbor magnetic exchange coupling but retains some form of electrical conductance through the pillar-like structure.

For simplicity one further assumes that both magnets are in their macrospin state with no internal magnetic degrees of freedom. This is equivalent to setting the exchange energy of the ferromagnets A_{ex} to be much larger than the energy scales involved in the problem for the given length scale of the structure. A convenient metric is for the exchange length λ_{ex} to satisfy [41, 42]

$$\lambda_{ex} = \sqrt{\frac{A_{ex}}{U_{an}}} \gg L \quad (2)$$

where A_{ex} is the exchange energy and U_{an} is the leading-order anisotropy energy density. For thin films with weak intrinsic or interface anisotropy, this is often the easy-plane anisotropy $2\pi M_s^2$ with M_s being the magnetization. For perpendicularly magnetized thin-film elements, U_{an} is the net perpendicular anisotropy. L is the largest dimension of the ferromagnet in the problem.

Torque and Dynamics of a Macrospin

A macrospin has only two degrees of freedom – those determining the direction of the magnetic moment. The dynamics of a macrospin is described by the Landau–Lifshitz–Gilbert (LLG) equation. In vector form, it is often written as [43]

$$\begin{aligned} \left(\frac{1}{\gamma}\right) \frac{d\mathbf{m}}{dt} &= \mathbf{m} \times \mathbf{H}_{\text{eff}} - \left(\frac{\alpha}{\gamma m}\right) \mathbf{m} \times \frac{d\mathbf{m}}{dt} \approx \\ &\approx \mathbf{m} \times \mathbf{H}_{\text{eff}} - \left(\frac{\alpha}{m}\right) \mathbf{m} \times (\mathbf{m} \times \mathbf{H}_{\text{eff}}) \end{aligned} \quad (3)$$

where the effective magnetic field \mathbf{H}_{eff} includes all torques from energy-conserving forces such as magnetic fields and anisotropy fields. For a fixed strength moment

\mathbf{m} in a given energy potential $U(\theta, \varphi)$, the effective field transverse to \mathbf{m} can be written as $\mathbf{H}_{\text{eff}} = -\nabla U = -(\partial U/\partial\theta) \mathbf{e}_\theta - (1/\sin\theta) (\partial U/\partial\varphi) \mathbf{e}_\varphi$, where \mathbf{e}_θ and \mathbf{e}_φ are unit vectors on the unit sphere of polar coordinates (θ, φ) ; for the θ and φ rotations, respectively, α is the phenomenological LLG damping constant and $\gamma \approx -2\mu_B/\hbar$ is the gyromagnetic ratio that converts between magnetic moment and angular momentum. The left-hand side of Eq. 3 is the time derivative of the total angular momentum of the macrospin and the right-hand side its corresponding driving force, i.e., the total torque acting on the macrospin. In this case the total torque includes that from \mathbf{H}_{eff} , which would be energy conserving if time independent, and a damping torque. Normally the energy-conserving torque term is orders of magnitude larger than the energy-nonconserving damping torque. The second line in Eq. 3 can therefore be viewed as a first-order iteration from the previous identity, assuming a small-damping torque term.

A Review of Spin-Containing Quantities and Spin Transport

Spin-1/2 Algebra

To facilitate the discussion in the next section, a brief review of spin-1/2 algebra is given here. Let Pauli matrices $\hat{\sigma}_1 = \begin{bmatrix} 0 & 1 \\ 1 & 0 \end{bmatrix}$, $\hat{\sigma}_2 = \begin{bmatrix} 0 & -i \\ i & 0 \end{bmatrix}$, and $\hat{\sigma}_3 = \begin{bmatrix} 1 & 0 \\ 0 & -1 \end{bmatrix}$ be the Cartesian components in spin space. Define a Pauli matrix vector

$$\hat{\boldsymbol{\sigma}} = \hat{\sigma}_x \mathbf{e}_x + \hat{\sigma}_y \mathbf{e}_y + \hat{\sigma}_z \mathbf{e}_z. \quad (4)$$

Then, one has

$$\begin{cases} [\hat{\sigma}_\mu, \hat{\sigma}_\nu]_+ = 0, \text{ i.e. } \hat{\sigma}_\mu \hat{\sigma}_\nu = -\hat{\sigma}_\nu \hat{\sigma}_\mu (\mu \neq \nu), (\mu, \nu) \in (x, y, z) \\ \hat{\sigma}_x \hat{\sigma}_y = i \hat{\sigma}_z (+ \text{cyclical permutations}). \\ \text{Tr}[\hat{\boldsymbol{\sigma}}_{x,y,z}] = 0 \\ \hat{\sigma}_{x,y,z}^2 = \hat{I} \end{cases}. \quad (5)$$

where \hat{I} , sometimes also denoted as $\hat{\sigma}_0$, is the 2×2 identity matrix. These properties give more generally for any unit vector \mathbf{n} , $(\mathbf{n} \cdot \hat{\boldsymbol{\sigma}})^2 = \hat{I}$. Also, given two vectors \mathbf{A} and \mathbf{B} in real space,

$$(\mathbf{A} \cdot \hat{\boldsymbol{\sigma}})(\mathbf{B} \cdot \hat{\boldsymbol{\sigma}}) = (\mathbf{A} \cdot \mathbf{B})\hat{I} + i(\mathbf{A} \times \mathbf{B}) \cdot \hat{\boldsymbol{\sigma}}. \quad (6)$$

A spin of direction \mathbf{n} is representable in spin space by a 2×2 matrix as

$$\hat{S}_n = \left(\frac{\hbar}{2}\right)(\mathbf{n} \cdot \hat{\boldsymbol{\sigma}}) = \left(\frac{\hbar}{2}\right) \sum_\nu S_{n,\nu} \hat{\sigma}_\nu. \quad (7)$$

Its expectation value along any unit vector direction \mathbf{n}' is therefore

$$\langle S_{n,n'} \rangle = \left(\frac{\hbar}{4} \right) \text{Tr}[(\mathbf{n} \cdot \hat{\sigma}) (\mathbf{n}' \cdot \hat{\sigma})]. \quad (8)$$

Consequently a real-space expectation value of total spin in vector form is

$$\langle \mathbf{S}_n \rangle = \frac{1}{2} \text{Tr}[\hat{S}_n \hat{\sigma}]. \quad (9)$$

Considerations for Quantitative Description of Spin Transport

For combined charge- and spin-carrying transport problems in solids, following the approaches of Stiles and Zangwill [15], one can draw an analogy between the conventional particle (charge) current transport and that of the spin current. For charged particle transport, one writes the number density $n(\mathbf{r})$, the particle number current $\mathbf{j}(\mathbf{r})$, and the current continuation relationship as

$$\begin{cases} n(\mathbf{r}) = \sum_{i,\sigma} \psi_{i,\sigma}^*(\mathbf{r}) \psi_{i,\sigma}(\mathbf{r}) \\ \mathbf{j}(\mathbf{r}) = \text{Re} \left[\sum_{i,\sigma} \psi_{i,\sigma}^*(\mathbf{r}) \hat{\mathbf{v}} \psi_{i,\sigma}(\mathbf{r}) \right] \\ \nabla \cdot \mathbf{j} + \frac{\partial n}{\partial t} = 0 \end{cases} \quad (10)$$

with $\psi_{i,\sigma}$ as an occupied single-particle wave function with state index i and spin index σ and $\hat{\mathbf{v}} = -(i\hbar/m) \nabla$ as the velocity operator. \mathbf{r} is the real-space coordinate vector.

To keep track of the spin component of the transport carriers, one recalls, for example, in Ref. [44] that a spin-1/2 eigenstate along an arbitrary real-space unit vector direction \mathbf{n}_s can be represented in spin space by a 2×2 matrix of $\mathbf{n}_s \cdot \hat{\sigma} = \hat{\sigma}_1 (\mathbf{e}_x \cdot \mathbf{n}_s) + \hat{\sigma}_2 (\mathbf{e}_y \cdot \mathbf{n}_s) + \hat{\sigma}_3 (\mathbf{e}_z \cdot \mathbf{n}_s)$, where $\hat{\sigma} = \hat{\sigma}_1 \mathbf{e}_x + \hat{\sigma}_2 \mathbf{e}_y + \hat{\sigma}_3 \mathbf{e}_z$ is a vector matrix with the three Pauli matrices $\hat{\sigma}_1 = \begin{bmatrix} 0 & 1 \\ 1 & 0 \end{bmatrix}$, $\hat{\sigma}_2 = \begin{bmatrix} 0 & -i \\ i & 0 \end{bmatrix}$, and $\hat{\sigma}_3 = \begin{bmatrix} 1 & 0 \\ 0 & -1 \end{bmatrix}$ as its Cartesian basis set that defines the spin space. One may then write out for spin-1/2 particles the spin-density matrix $\hat{\mathbf{m}}$, the spin-current tensor $\hat{\mathbf{Q}}(\mathbf{r})$, and spin-current continuity relationship as

$$\begin{cases} [\hat{\mathbf{m}}(\mathbf{r})]_{\sigma,\sigma'} = \sum_i \psi_{i,\sigma}^*(\mathbf{r}) \hat{\mathbf{s}}_{\sigma,\sigma'} \psi_{i,\sigma'}(\mathbf{r}) \\ [\hat{\mathbf{Q}}(\mathbf{r})]_{\sigma,\sigma'} = \text{Re} \left[\sum_i \psi_{i,\sigma}^*(\mathbf{r}) \hat{\mathbf{s}}_{\sigma,\sigma'} \otimes \hat{\mathbf{v}} \psi_{i,\sigma'}(\mathbf{r}) \right] \\ \nabla \cdot \hat{\mathbf{Q}} + \frac{\partial \hat{\mathbf{m}}}{\partial t} = -\frac{\delta \hat{\mathbf{m}}}{\tau_{\uparrow\downarrow}} + \hat{\mathbf{n}}_{\text{ext}} \end{cases} \quad (11)$$

where $\hat{\mathbf{s}} = (\hbar/2)\hat{\boldsymbol{\sigma}}$, and $\nabla \cdot \hat{\mathbf{Q}} = \frac{\partial \hat{Q}_{ik}}{\partial k}$ (sum over repeated indices $k = \{x, y, z\}$) is a 2×2 matrix with its left index i for its Cartesian axes in spin space, as is the spin density $\hat{\mathbf{m}}$, originating from $\hat{\mathbf{s}}$ as described above. The last equation in Eq. 11 is the spin-current continuity relation, where $\tau_{\uparrow\downarrow}$ is the spin-flip scattering lifetime, $\delta\hat{\mathbf{m}} = \hat{\mathbf{m}} - \hat{\mathbf{m}}_{\text{equilibrium}}$ is the so-called spin accumulation, and $\hat{\mathbf{n}}_{\text{ext}}$ includes all externally delivered spin current. Here $\square_{\sigma, \sigma'}$ represents a matrix element in the 2×2 spin space.

In this form, $\hat{\mathbf{m}}(\mathbf{r})$ is a vector matrix in real space with the 2×2 matrix indexed in spin space. The choice of $\psi_{i, \sigma}$ for diagonalizing the corresponding Hamiltonian, when possible, would dictate a real-space spin eigenstate axis \mathbf{n}_s for $\{\sigma, \sigma'\}$ to be “good” quantum numbers. Then the 2×2 matrix $[\mathbf{n}_s \cdot \hat{\mathbf{m}}]_{\sigma, \sigma'}$ becomes a description of $\hat{\mathbf{m}}$ in spin space defined by direction \mathbf{n}_s in real space.

The projections of the spin density $\hat{\mathbf{m}}$ along $(\mathbf{e}_x, \mathbf{e}_y, \mathbf{e}_z)$ are $\langle m_\beta \rangle = (1/2) \text{Tr} [\hat{\mathbf{m}}\hat{\sigma}_\beta]$ for $\beta = (x, y, z)$ [44], giving the total average spin angular momentum density as

$$\langle \mathbf{m} \rangle = \left(\frac{1}{2} \right) \text{Tr} [\hat{\mathbf{m}}\hat{\boldsymbol{\sigma}}]. \quad (12)$$

The charge and spin current can often be conveniently combined into a 2×2 matrix vector form by joining Eqs. 10 and 11 to read [45, 46]

$$\hat{\mathbf{i}} = \left(\frac{e}{2} \right) \mathbf{j}\hat{\sigma}_0 - \left(\frac{e}{\hbar} \right) \hat{\mathbf{Q}} \quad (13)$$

with $\hat{\sigma}_0 = \begin{bmatrix} 1 & 0 \\ 0 & 1 \end{bmatrix}$, so that $\text{Tr} [\hat{\mathbf{i}}]$ gives the charge-current component, while the traceless part of the matrix gives the spin current. In situations such as ballistic transport limit where a spin current with a unique spin eigenstate can be identified, this reduces to the form used in Ref. [46]

$$\hat{\mathbf{i}} = \frac{1}{2} \mathbf{j}\hat{\sigma}_0 - \left(\frac{e}{\hbar} \right) \mathbf{n}_s \cdot \hat{\boldsymbol{\sigma}} \quad (14)$$

where \mathbf{n}_s describes the orientation of the spin current’s eigenstate orientation in real space. In this situation the local electrochemical potentials μ_c (scalar) and spin-accumulation potential $\boldsymbol{\mu}_s$ (real-space vector) can be written as

$$\mu_c = \int_{\varepsilon_0}^{\infty} \text{Tr} [\hat{f}(\varepsilon)] d\varepsilon \quad (15)$$

and

$$\boldsymbol{\mu}_s = \int_{\varepsilon_0}^{\infty} \text{Tr} [\hat{f}(\varepsilon)\hat{\boldsymbol{\sigma}}] d\varepsilon \quad (16)$$

with $\hat{f}(\varepsilon) = f_{FD}(\varepsilon) \hat{\sigma}_0$ and with $f_{FD}(\varepsilon) = \left[\exp\left(\frac{\varepsilon - \varepsilon_F}{k_B T}\right) + 1 \right]^{-1}$ being the Fermi distribution function. This in linear response limit reduces the relationship between a spin-accumulation density vector $\delta \mathbf{m}$ and the spin-accumulation potential μ_s as

$$\delta \mathbf{m} = \frac{1}{2} \text{Tr} [(\delta \hat{\mathbf{m}}) \hat{\sigma}] = (\hbar/2) N(\varepsilon_F) \mu_s \quad (17)$$

with $N(\varepsilon_F)$ as the density of states at the Fermi level [46]. Equations 14, 15, 16, and 17 are most convenient when describing steady-state spins in a nonmagnetic metal or in a ferromagnet with collinear spin moment alignment.

For a ferromagnet in noncollinear arrangement with electron spins, the exchange field would result in rapid precession of spin states both in space and in time, making the values of Eqs. 14, 15, 16, and 17 difficult to evaluate or interpret.

In a nonmagnetic metal, on the other hand, Eqs. 14, 15, 16, and 17 can give well-defined spin-current magnitude, eigenstate directions, and current directions into and out of a normal metal–ferromagnetic metal interface. An appropriate summation of these spin currents together with spin angular momentum conservation could lead to the amount of torque absorbed by the ferromagnets in question.

Origins of Spin Torque

Spin Valves and a Normal Metal–Ferromagnetic Metal Interface

To examine the effect of spin-dependent transport across a ferromagnet–nonmagnetic materials interface, one needs to apply Eq. 11 for each individual transport channel’s wave function, keeping account in both momentum and spin space. To illustrate the concepts with a simple case, assume a metallic $\parallel \text{NIF}_1 | \text{NIF}_2 | \text{N} \parallel$ spin-valve type of junction stack as depicted in Fig. 2. Assume transport involves only simple free-electron bands, with a large exchange splitting inside the ferromagnets F_1 and F_2 . This model, while simplistic, would be sufficient to reveal the origins of spin torque [14, 15].

Focus on the electrons entering F_2 while carrying spin magnetic moment in the direction $\mathbf{n}_s = \mathbf{n}_1$, where $\mathbf{n}_{1,2} = \mathbf{m}_{1,2}/m_{1,2}$ being the unit vector for the magnetic direction of $F_{1,2}$. Inside F_2 , the exchange splitting results in a different Fermi wavelength \mathbf{k}_F^\pm for the spin-up and spin-down states defined along \mathbf{n}_2 . This for a spin-carrying electron current with spin direction \mathbf{n}_s (generally noncollinear with \mathbf{n}_2) entering F_2 , when summed over all \mathbf{k} -vectors involved in transport across the NIF interface, results in a rapid oscillatory decoherence of the transverse spin amplitude inside F_2 – a situation addressed in the discussion surrounding Fig. 1.

This transverse spin angular momentum transfer would result in a torque in the direction of $\mathbf{m}_2 \times (\mathbf{m}_2 \times \mathbf{m}_1)$, which is in the plane of the incident electron’s spin-polarization direction \mathbf{m}_1 and that of the magnetic moment \mathbf{m}_2 ; thus it is also referred to as the “in-plane” spin torque or τ_{\parallel} [47]. This is the process described in Figs. 1 and 2 and is the simple physical picture of an electron spin-current-induced torque on a ferromagnet.

While this physical picture of the spin-transfer torque is simple, the quantitative calculation can quickly become rather complex. In principle the treatment needs to include spin-carrying electron transport channels in all directions, into and out of the ferromagnet on both front and back interfaces, summed over all states. Important issues such as the role of reflection and transmission amplitudes and phases of the electrons at two sides of each interfaces would be important for quantitative understandings [11, 14, 15].

For a simplified, symmetric film stack of $\parallel\text{N}|F_1|\text{N}|\text{N}|F_2|\text{N}\parallel$ where F_1 and F_2 are identical for the interfaces facing each other and its N|F interfaces do not have spin-current reflection from scattering of charge carriers, an in-plane spin torque of a transport current I induced on F_2 was calculated to be [11]

$$\boldsymbol{\tau}_{2\parallel} = \eta g(\mathbf{n}_1, \mathbf{n}_2) I \left(\frac{\hbar}{4e} \right) \mathbf{n}_2 \times (\mathbf{n}_2 \times \mathbf{n}_1) \quad (18)$$

with $\cos \theta = \mathbf{n}_1 \cdot \mathbf{n}_2$, where

$$\eta = \frac{I_P - I_{AP}}{I_P + I_{AP}} = \frac{G_P - G_{AP}}{G_P + G_{AP}}; \quad (19)$$

$$g(\mathbf{n}_1, \mathbf{n}_2) = g(\theta) = \frac{1}{\cos^2\left(\frac{\theta}{2}\right) + \left(\frac{r_s}{r_A}\right) \sin^2\left(\frac{\theta}{2}\right)}.$$

Here η is the charge-current spin polarization with current I or conductance G in the parallel (P), and antiparallel (AP) alignment between $F_{1,2}$. $r_A = A(R_P + R_{AP})/2$ is the average resistance-area product of the junction stack (A being its area); $r_s = \sqrt{3}\pi\hbar/e^2k_F^2 \approx 7.14 \times 10^{-4} \Omega\mu\text{m}^2$ is related to the Sharvin resistance [11, 48] of the N metal (r_s value here is for copper).

A similar discussion for the $F_1|\text{N}$ interface [49] shows a torque in the same direction acting on F_1 , forming a so-called ‘‘pinwheel’’ drive force on the two-layered magnetic stack formed by F_1 and F_2 . This nontrivial combination of torque characteristic of the in-plane spin-transfer torque could lead to dynamic excitations of both layers of magnets if they are of similar materials and with a similar thickness [49–52].

This discussion also highlights the subtle point of the sources of angular momentum current flow. The spin current in this case originates from the spin-flip relaxation processes, mostly from the leads outside the F_1 – F_2 structure.

Where multiple reflections of the carriers are expected [53], the angular dependence of τ_{\parallel} can be different from Eq. 19. One such example is theoretically discussed in Ref. [54]. It may also be possible that a reflected carrier has its spin eigenstate in a direction different from either \mathbf{m}_1 or \mathbf{m}_2 , which could in principle cause more complex situations to develop. Although in reality the dephasing of reflected electron’s spin state tends to be strong, hence the assumption is often made for it to possess the spin direction of the last ferromagnet interface from which it reflects [15, 53].

Magnetic Tunnel Junction and a Tunnel Barrier Interface for Spin Transport

In the case of spin-polarized tunneling, the middle nonmagnetic separation layer between F_1 and F_2 is replaced by an insulating tunnel barrier. For such $\|N|F_1\rangle\langle F_2|N\rangle\|$ structure and at a small, constant voltage bias across the stack, the charge conductances for parallel (P) and antiparallel (AP) alignment are calculated to be [13, 40, 47]

$$G_P = G_{++} + G_{--}, G_{AP} = G_{+-} + G_{-+} \quad (20)$$

while the spin current gives an in-plane spin-transfer torque on F_2 that amounts to $\tau_{2\parallel}$, with

$$\frac{d\tau_{2\parallel}}{dV} \approx \left(\frac{\hbar}{4e}\right) (G_{++} - G_{--} + G_{+-} - G_{-+}) \mathbf{n}_2 \times (\mathbf{n}_2 \times \mathbf{n}_1) \quad (21)$$

where $G_{i,j}$ with $(i,j) \in \{-,+\}$ are the tunnel conductance matrix elements between spin eigenstates of F_1 and F_2 in two collinear alignment geometries: $G_{++}(G_{--})$ are for left (F_1) majority (minority) to right (F_2) majority (minority) density of states, G_{-+} and G_{+-} are for left (F_1) minority to right (F_2) majority density of states, and so on. The small voltage assumption is such that the conductance matrices are not strongly voltage dependent, and the constant voltage assumption is such that the voltage across the tunnel barrier is independent of the magnitude of the charge-current flow.

Using the definition of magnetoresistance $m_r = (R_{AP} - R_P)/R_P$ where $R_P, R_{AP} = 1/G_P, G_{AP}$ are junction resistances in P and AP states and for very high tunnel magnetoresistance such as those seen in MgO-based devices [32, 40], one may assume $G_{++} \gg \{G_{+-}, G_{-+}\} \gg G_{--}$ [40]. In this limit and assuming symmetric electrode and interfaces, one arrives at an estimate of the in-plane spin torque in relation to observable TMR values m_r in the form of [40]

$$\begin{aligned} \frac{d\tau_{2\parallel}}{dV} &\approx \left(\frac{\hbar}{4e}\right) G_P \frac{2P}{1+P^2} \mathbf{n}_2 \times (\mathbf{n}_2 \times \mathbf{n}_1) = \\ &= \left(\frac{\hbar}{4e}\right) G_P \frac{\sqrt{m_r(m_r+2)}}{m_r+1} \mathbf{n}_2 \times (\mathbf{n}_2 \times \mathbf{n}_1) \end{aligned} \quad (22)$$

where $P = \sqrt{\frac{G_P - G_{AP}}{G_P + G_{AP}}} = \sqrt{\frac{m_r}{m_r + 2}}$. Note for this definition that $m_r = (R_{AP} - R_P)/R_P \in [0, +\infty]$. Readers are encouraged to compare Eq. 22 with that of the spin-valve expression, Eqs. 18 and 19.

Generalized Parameterization and the Concept of a ‘‘Mixing Conductance’’

The spin-transport problem described above can sometimes be simplified and generalized to a phenomenological ‘‘lumped element’’ circuit-like model, where

the various ferromagnetic and nonmagnetic volumes (nodes) are connected via idealized interfaces supporting spin-dependent, ballistic transmission and reflection of carrier electrons [45, 46, 55]. Such interface connection is similar to the mesoscopic ballistic charge transport models of Landau and Büttiker [56, 57]. These allow direct identification of the spin eigenstate components of the various currents entering and leaving a specific volume, providing a quantitative description of the spin torque acting on such volumes if they are ferromagnetic. Within these assumptions, the charge and spin current realizes their simplified forms as described by Eq. 27 in Ref. [46], and for an NIF interface, the total spin torque associated with transport across this particular interface can be written as

$$\boldsymbol{\tau} \approx \frac{1}{4\pi} \left(g_r^{\uparrow\downarrow} \mathbf{m} \times (\boldsymbol{\mu}_s \times \mathbf{m}) + g_i^{\uparrow\downarrow} \boldsymbol{\mu}_s \times \mathbf{m} \right) \quad (23)$$

where the first term is the τ_{\parallel} in notations used here. The second term describes a field-like or perpendicular torque $\boldsymbol{\tau}_{\perp}$ due to the reflection or incomplete absorption of transverse spin angular momentum, as discussed conceptually in section “[Metal-to-Metal Interface and Spin Valves](#).” The spin-potential vector $\boldsymbol{\mu}_s$ is defined by Eq. 16 in the normal metal adjacent to the ferromagnet in question. The quantities and $g_r^{\uparrow\downarrow}$ and $g_i^{\uparrow\downarrow}$ are the so-called mixing conductances. For typical metal spin valves, $g_r^{\uparrow\downarrow} \gg g_i^{\uparrow\downarrow}$ [46], thus only τ_{\parallel} is significant.

Modified LLG Equation with a Spin-Torque Term

The microscopic mechanisms discussed in sections “[A Review of Spin-Containing Quantities and Spin Transport](#)” and “[Origins of Spin Torque](#)” introduces a transport-induced, energy-nonconserving torque term into a macrospin’s dynamic equation, the so-called Slonczewski spin-transfer torque or in-plane torque, τ_{\parallel} , as detailed by Eqs. 18 and 22. Combining them with Eq. 3, one has the modified LLG equation including the in-plane spin torque for the magnet with moment \mathbf{m} receiving spin torque τ_{\parallel} (which is formerly also called F_2 earlier in this chapter) to be

$$\left(\frac{1}{\gamma} \right) \frac{d\mathbf{m}}{dt} = \mathbf{m} \times \mathbf{H}_{\text{eff}} - \left(\frac{\alpha}{\gamma m} \right) \mathbf{m} \times \frac{d\mathbf{m}}{dt} + \left(\frac{I_s}{m^2} \right) \mathbf{m} \times (\mathbf{m} \times \mathbf{n}_s) \quad (24)$$

where I_s is the spin-current amplitude and can be written as

$$I_s = \left(\frac{\hbar I}{2e} \right) \left(\frac{G_P - G_{AP}}{G_P + G_{AP}} \right) \frac{1}{2 \left[\cos^2 \left(\frac{\theta}{2} \right) + \left(\frac{r_s}{r_A} \right) \sin^2 \left(\frac{\theta}{2} \right) \right]} \quad (25)$$

for all-metal spin valves from Eq. 18 and

$$I_s = \left(\frac{\hbar}{2e} \right) G_p V \frac{\sqrt{m_r(m_r + 2)}}{2(m_r + 1)} \quad (26)$$

for tunnel junctions with symmetric leads and barrier interfaces with high MR and at low bias voltage, following Eq. 22. \mathbf{n}_s of course is the spin-polarization direction of the spin current I_s . Note that in this expression of Eq. 24, the general form of I_s could contain dependences on the relative orientation between the incoming spin current's spin-polarization direction \mathbf{n}_s and the local moment \mathbf{m} under description, especially so for the spin-valve case explicitly described in Eq. 25.

For other forms of spin current such as a spin current at a ferromagnet–non-magnetic interface originating from a spin accumulation induced by a charge current that does not necessarily traverse the same interface (the so-called nonlocal spin-current geometry [58–60]), the angular dependence of I_s entering the free layer's LLG equation may be different from Eqs. 25 or 26, depending on the details of the interface and metal layer transmission and reflection properties for conduction channels of different spin components. One such model system is shown in Ref. [45].

For small α and comparably small τ_{\parallel} , Eq. 24 can be iterated once to read

$$\left(\frac{1}{\gamma} \right) \frac{d\mathbf{m}}{dt} = \mathbf{m} \times \mathbf{H}_{\text{eff}} - \left(\frac{\alpha}{m} \right) \mathbf{m} \times (\mathbf{m} \times \mathbf{H}_{\text{eff}}) + \left(\frac{I_s}{m^2} \right) \mathbf{m} \times (\mathbf{m} \times \mathbf{n}_s) \quad (27)$$

which explicitly brings out the similarity between the in-plane spin-torque term and the damping term in vector form.

Spin-Torque-Induced Magnetodynamics

Time Scales, Length Scales, and Constitutive Relationship for Spin-Torque Dynamics in Continuous Medium

One implicit assumption in the formulation in section “Origins of Spin Torque” (and especially section “Modified LLG Equation with a Spin-Torque Term”) is that the transport processes producing the spin torque τ_{\parallel} can be treated with a stationary moment configuration for $\mathbf{m}_{1,2}$, and the resulting torque expression would be usable for describing the dynamics of the magnetic moment \mathbf{m} in Eqs. 24, 25, 26, and 27. The justification for this approximation lies in the separation of time scales between the macroscopic motion of the ferromagnetic moment \mathbf{m} and the time-dependent dynamics the spin-carrying transport carriers experience. Fundamentally these time scales are related to the energy potentials producing \mathbf{H}_{eff} in LLG Eqs. 24 or 27 and the exchange-splitting energy at play in determining the transport carrier's dynamics. The former usually involves magnetic fields no larger than a few teslas (hence

an energy scale of $2\mu_B H \sim 10^{-4}$ eV), whereas the exchange splitting for conduction electrons could easily be of the order of 1 eV. The \mathbf{H}_{eff} precession dynamics, at 2.8 GHz/kOe, is therefore thousands of times slower than that of the transport carrier dynamics. Therefore, a spin torque derived using a stationary \mathbf{m} treatment could usually be applied to the magnetodynamics of \mathbf{m} in the simple form as stated by Eqs. 24, 25, 26, and 27.

One area this approximation may break down is when the system temperature becomes sufficiently high and when one is interested in the details of magnetic fluctuations with the presence of spin current. In this case, thermal energy may cause the fluctuations of the carrier systems to affect that of the total magnetic moment in ways that blur the boundary of time scales for such approximations.

Up till now for spin torque, one had also assumed the magnets involved were macrospins. In reality, internal magnetic degrees of freedom of the magnets such as $F_{1,2}$ in a layered pillar structure as those described in Fig. 2 do have significant influence on the overall behavior of such structures under spin torque. A phenomenological way of including a magnet's internal degrees of freedom is to explicitly include the long-wavelength magnetic exchange-stiffness term in the LLG equation. Following Landau and Lifshitz [61] or Herring and Kittel [43], one may make the LLG Eq. 3 position dependent through the substitutions of $\mathbf{m} \rightarrow \mathbf{m}(\mathbf{r})$ and $\mathbf{H}_{\text{eff}} \rightarrow \mathbf{H}_{\text{eff}}(\mathbf{r})$. The exchange stiffness can then be treated as a local force related to the spatial variation of the local magnetic moment direction: $\mathbf{H}_{\text{eff}}(\mathbf{r}) \rightarrow \mathbf{H}_{\text{eff}}(\mathbf{r}) + \left(\frac{D}{2\mu_B m}\right) \nabla^2 \mathbf{m}(\mathbf{r})$, which after Fourier transforming the LLG equation into its corresponding momentum space would read

$$\mathbf{H}_{\text{eff}}(\mathbf{k}) \rightarrow \mathbf{H}_{\text{eff}}(\mathbf{k}) + \left(\frac{D}{2\mu_B}\right) \mathbf{k}^2 \quad (28)$$

where $D = (2\hbar\gamma/M_s) A_{ex} = (4\mu_B/M_s) A_{ex}$ is the exchange-stiffness constant (e.g., $D \sim 0.5 \text{ eV}\text{\AA}^2$ for cobalt [62]).

More generally, the phenomenological LLG equation for a magnetic body may be rewritten as

$$\begin{aligned} \left(\frac{1}{\gamma}\right) \frac{d\mathbf{m}(\mathbf{r})}{dt} &= \mathbf{m}(\mathbf{r}) \times \left[\sum_{\mathbf{r}'} \mathbf{H}_{\text{eff}}(\mathbf{r}, \mathbf{r}') + \left(\frac{D}{2\mu_B m}\right) \nabla^2 \mathbf{m}(\mathbf{r}) \right] - \\ &- \left[\frac{\alpha}{\gamma m(\mathbf{r})} \right] \mathbf{m}(\mathbf{r}) \times \frac{d\mathbf{m}(\mathbf{r})}{dt} + \sum_{\mathbf{r}'} \boldsymbol{\tau}_{\parallel}(\mathbf{r}, \mathbf{r}') \end{aligned} \quad (29)$$

Note that while the exchange stiffness may be adequately treated as a local interaction within the LLG equation, other torque terms, most notably that of the dipolar interaction from different regions of the magnet of concern, may be nonlocal in nature. This is also true for the spin-torque term that $\boldsymbol{\tau}_{\parallel}$, $\boldsymbol{\tau}_{\parallel}$ may be

nonlocal because spin current in the nonmagnetic layer N could diffuse in the film plane along the interface as well. The same could happen within the ferromagnets $F_{1,2}$, especially if one includes magnon scattering of conduction electrons. This for magnetically inhomogeneous NIF interfaces could induce spin currents not just between $F_{1,2}$ but laterally between different regions of F_1 and F_2 . Such lateral spin currents are particularly important for all-metal spin-valve structures, where the lateral electrical conductivity of the N layer is highly relative to the interface resistance at NIF. The damping term could in principle become nonlocal, too, especially when one considers the precession-related electrical voltage effects known as spin pumping [63–65].

These nonlocal interactions involve different length scales and functional forms. The dipolar interaction is long range, following a $|\mathbf{r} - \mathbf{r}'|^{-2}$ force dependence. This is a well-known difficulty in treating micromagnetic problems. The spin-current-related nonlocal interactions are generally more complex but tend to be truncated by spin–flip scattering processes which usually decays exponentially in distance with a characteristic length scale of l_{sf} , a materials parameter, usually related to the strength of spin–orbit interaction of the material. High-energy magnon-mediated spin–flip scattering could be more complex, although that could in principle also be included phenomenologically in the relevant parameters of l_{sf} of the material. The combined effects of these nonlocal interactions tend to be rather difficult to capture except for a few very special cases. Numerical simulations, on the other hand, could include these interactions if necessary but at the expense of computation intensity. A special class of problem attracting a lot of practical interests is the effect of spin current on the motion of magnetic domain walls. Such discussion is however beyond the scope of this chapter. Readers are referred to, for example, Ref. [66] for further discussion.

The quantity l_{sf} can vary widely depending on materials and structures. In a nonmagnetic metal such as Cu, the zero-temperature l_{sf} can be of the order of 1 μm . It decreases to about 100 nm at room temperature. Normally l_{sf} would decrease for heavier elements due to the rapid increase of spin–orbit scattering. Interfaces and atomic disorder can result in additional spin–flip scattering, reducing the effective l_{sf} . In ferromagnets and antiferromagnets, l_{sf} is usually much shorter and often difficult to define and measure for some materials due to the importance of interface and atomic ordering that are difficult to control. l_{sf} is more generally related to the spin lifetime τ_{sf} of the electronic states involved. The exact conversion between these two quantities would depend on the details of the electronic transport of the states involved and is beyond the scope of this review.

The hierarchy of the length scales is often such that the exchange length λ_{ex} as expressed in Eq. 2 plays a central role in determining the complexity of the LLG equation involved. This is because $\mathbf{m}(\mathbf{r})$ would vary appreciably over a length scale of the order of exchange length. Hence if the problem only has length scales shorter than λ_{ex} , most of the spatial dependence issues go away, and the LLG is reduced to its simpler form of Eq. 24. For modern materials of technological interest such as

the perpendicularly magnetized ultrathin CoFeB thin films forming part of the MgO-based magnetic tunnel junction, λ_{ex} is usually well below 50 nm.

Zero-Temperature Macrospin Dynamics

The basic dynamics resulting from a spin torque τ_{\parallel} can be illustrated with a zero-temperature macrospin model based on Eq. 24. For simplicity one may assume the spin current I_s is with a fixed polarization direction \mathbf{n}_s , and the magnitude of I_s does not depend on the relative angle of the magnetic moment \mathbf{m} with \mathbf{n}_s – an assumption that would be modified for a spin-valve geometry as will soon be discussed below. One further assumes the simplest case where all magnetic axes including the spin-polarization direction, the applied magnetic-field direction, and the anisotropy field direction (if any) are one and the same. With this collinear alignment, the LLG equation Eq. 24 can be examined analytically for some special cases.

One of the simplest special cases is if the only energy-conserving force present in the question is a collinear-applied magnetic field along unit vector direction \mathbf{e}_z . In this case the small-damping LLG equation with spin torque, Eq. 27, can be rewritten as

$$\begin{aligned} \left(\frac{1}{\gamma}\right) \frac{d\mathbf{m}}{dt} &= \mathbf{m} \times H\mathbf{e}_z - \left(\frac{\alpha}{m}\right) \mathbf{m} \times (\mathbf{m} \times H\mathbf{e}_z) + \left(\frac{I_s}{m^2}\right) \mathbf{m} \times (\mathbf{m} \times \mathbf{e}_z) = \\ &= \mathbf{m} \times H\mathbf{e}_z - \left(\frac{\tilde{\alpha}}{m}\right) \mathbf{m} \times (\mathbf{m} \times H\mathbf{e}_z) \end{aligned} \quad (30)$$

with $\tilde{\alpha} = \alpha - I_s/mH$. The last line in Eq. 30 recovers a normal LLG equation form Eq. 3 without explicit spin-torque terms but now with a spin-current-controlled apparent damping coefficient $\tilde{\alpha}$.

The leading-order effect of the spin torque can readily be deduced from Eq. 30. The effect of the spin torque is seen here as to modify the apparent damping of the macrospin dynamics. Depending on the sign and magnitude of the spin current, it could cause the apparent damping coefficient $\tilde{\alpha}$ to become larger or smaller than the materials LLG damping α or even to reverse sign. When $\tilde{\alpha}$ changes sign into negative values, the macrospin's precession is no longer damped but rather amplified, resulting in an increase of the precession cone angle over time. Thus, the point of $\tilde{\alpha} = 0$ is a critical instability threshold, and it defines the threshold spin current for inducing magnetic excitation and even magnetic reversal. The threshold spin current thus defined has the form $I_{s,\text{critical}} = mH\alpha$.

For a macrospin in a strong collinear uniaxial anisotropy energy well, $H_{\text{eff}} = H_k \cos \theta$ with $\cos \theta = \mathbf{n}_m \cdot \mathbf{n}_H$. The dynamics near the bottom of the well of $\theta \approx 0$ is not significantly different from a unidirectional field discussed above. Thus

$$I_{s,\text{critical}} = \alpha m(H + H_k). \quad (31)$$

Translating this into its corresponding charge current, one has the threshold critical current expression

$$I_c = \left(\frac{2e}{\hbar}\right) \left(\frac{\alpha}{\tilde{\eta}}\right) m(H + H_k) \quad (32)$$

where

$$\tilde{\eta} = \left(\frac{G_P - G_{AP}}{G_P + G_{AP}}\right) \frac{1}{2 \left[\cos^2\left(\frac{\theta}{2}\right) + \left(\frac{r_s}{r_A}\right) \sin^2\left(\frac{\theta}{2}\right) \right]} \quad (33)$$

for all-metal spin valves such as ColCulCo. This relation follows directly from Eq. 25. Here instead of assuming a charge current with angle-independent spin polarization passing through the nanomagnet, the expression for $\tilde{\eta}$ already includes a realistic symmetric spin-valve transport model [11] for converting a spin-current threshold back to a charge-current threshold.

This threshold I_c may be generally asymmetric for P-AP state, corresponding to a $\theta = 0$ initial state, and AP-P state, corresponding to an initial $\theta = \pi$.

For high TMR tunnel junctions, the instability threshold in the term bias voltage reads

$$V_c = \left(\frac{2e}{\hbar}\right) \left(\frac{\alpha}{G_P}\right) \frac{2(m_r + 1)}{\sqrt{m_r(m_r + 2)}} m(H + H_k) \quad (34)$$

which follows from Eq. 26. This threshold is symmetric in voltage for the P-AP and AP-P transitions rather than in current, i.e., the same parallel state conductance factor G_P enters the threshold expression for both configurations. This is also a result of the spinor transformation and its related consequences on transport conductance matrices [13, 39, 40]. If one writes for an MTJ the P-AP transition threshold current as $I_{c, P-AP} = G_P V_c$, one could reuse Eq. 32, with an effective polarization factor of

$$\tilde{\eta} = \sqrt{m_r(m_r + 2)}/2(m_r + 1) \quad (35)$$

However, use caution since the AP-P transition threshold current would be much less, corresponding to $I_{c, AP-P} = G_{AP} V_c$.

The difference in angular dependence of the torque between a spin valve and an MTJ is due to the difference of impedances between the two ferromagnetic electrodes with respect to the full stack. In a spin valve the impedances are similar, and a change in magnetoresistance results in different voltage distributions which affects spin accumulation and thus spin polarization of the currents flowing through the relevant interfaces. For an MTJ, the tunnel interfaces' impedance is assumed to

be much larger than the rest of the pillar. Thus, the spin-accumulation-related corrections to total voltage from the rest of the pillar are negligible in most practical situations.

The instability thresholds Eqs. 32 and 34 can also be more carefully derived using a small cone-angle-linearized LLG equation including all anisotropy terms. One important case is the situation of a thin-film nanomagnet with a uniaxial anisotropy axis lying in the film plane and a strong easy-plane demagnetization field $4\pi M_s$ as dictated by the thin-film shape. In this case one replaces the $m(H + H_k)$ term in Eqs. 32 and 34 with $m(H + H_k + 2\pi M_s)$ [14, 20, 21].

The instability threshold is only a threshold for small cone-angle instability. It does not necessarily lead to a full reversal of the magnetic moment direction in general. However, in these two special situations discussed above (with simple uniaxial anisotropy alone or a combined uniaxial and easy-plane anisotropy) and at applied fields smaller compared to anisotropy energy scales, it turns out this instability does lead to a full reversal of the magnetic moment later in time.

Another simple case to examine is if the spin-polarization direction \mathbf{n}_s in Eqs. 24 or 27 is not collinear with that of the uniaxial and applied field direction \mathbf{e}_z , but with $\mathbf{n}_s \cdot \mathbf{e}_z = \cos \phi$. In this case the critical spin current Eq. 31 and the resulting critical charge current or voltage Eqs. 32 and 34 would pick up an additional factor of $1/\cos \phi$ [20, 21, 67]. This divergence of the threshold current with respect to the tilt angle when $\phi \rightarrow \pi/2$ might be counterintuitive at first. It results from a partial cancellation of the total transferred spin angular momentum for a portion of the precession orbit of \mathbf{m} when $\phi \neq 0$. [21, 67].

These instability solutions derived above do not include effects of finite temperature which is important for nanomagnet dynamics, as will be described in sections below.

Finite-Temperature Macrospin Dynamics

LLG Equation with a Langevin Field for Finite-Temperature Dynamics

At finite temperature and in thermal equilibrium with a thermal bath, a macrospin will have a finite probability of being found near its energy potential minimum with a probability described by the Boltzmann distribution. The time-dependent LLG equation for such a system can be written as

$$\left(\frac{1}{\gamma}\right) \frac{d\mathbf{m}}{dt} = \mathbf{m} \times (\mathbf{H}_{\text{eff}} + \mathbf{H}_L) - \left(\frac{\alpha}{m}\right) \mathbf{m} \times (\mathbf{m} \times \mathbf{H}_{\text{eff}}) \quad (36)$$

which is similar to the zero-temperature Eq. 3's \mathbf{H}_{eff} but with an additional white-spectrum random vector field \mathbf{H}_L (also called the Langevin field) to describe the thermal fluctuation due to interaction with the thermal bath. One may write $\mathbf{H}_L = H_{Lx}\mathbf{e}_x + H_{Ly}\mathbf{e}_y + H_{Lz}\mathbf{e}_z$ in Cartesian coordinates, with the three components

satisfying $\langle H_{Li} \rangle = 0$ and $\langle H_{Li}H_{Lj} \rangle = H_L^2 \delta_{i,j}$ where $\{i,j\} \in \{x,y,z\}$, and with the amplitude H_L determined through the fluctuation–dissipation relationship, giving a \mathbf{H}_L relating to the system temperature T as $H_{L,i} = \sqrt{2\alpha k_B T / \gamma m} I_{\text{ran},i}(t)$ ($i = x, y, z$), where $I_{\text{ran}}(t)$ is a Gaussian random function with the first two moments of $\langle I_{\text{ran}}(t) \rangle = 0$ and $\langle I_{\text{ran}}^2(t) \rangle = 1$, with the three components' fluctuation being uncorrelated [68].

With the presence of in-plane spin torque $\boldsymbol{\tau}_{\parallel}$, if one assumes the spin-torque term is without fluctuation, one may rewrite Eq. 36 in the same way as Eq. 27:

$$\left(\frac{1}{\gamma}\right) \frac{d\mathbf{m}}{dt} = \mathbf{m} \times (\mathbf{H}_{\text{eff}} + \mathbf{H}_L) - \left(\frac{\alpha}{m}\right) \mathbf{m} \times (\mathbf{m} \times \mathbf{H}_{\text{eff}}) + \left(\frac{I_s}{m^2}\right) \mathbf{m} \times (\mathbf{m} \times \mathbf{n}_s). \quad (37)$$

Note this is a leading-order expression, thus higher-order terms of H_L are ignored here.

An interesting case arises when \mathbf{H}_{eff} contains only a magnetic field and is in collinear alignment as assumed in Eq. 30:

$$\left(\frac{1}{\gamma}\right) \frac{d\mathbf{m}}{dt} = \mathbf{m} \times (\mathbf{H}_{\text{eff}} + \mathbf{H}_L) - \left(\frac{\tilde{\alpha}}{m}\right) \mathbf{m} \times (\mathbf{m} \times \mathbf{H}_{\text{eff}}) \quad (38)$$

where the apparent damping coefficient $\tilde{\alpha} = \alpha - I_s/mH$ assumes the spin-current-modified value. A fluctuation-free spin current would not change \mathbf{H}_L , and thus one is led to a fictitious temperature \tilde{T} in the presence of a spin torque such that $\sqrt{2\alpha k_B T / \gamma m} = \sqrt{2\tilde{\alpha} k_B \tilde{T} / \gamma m}$, thus giving the fictitious temperature as a function of the spin current:

$$\tilde{T} = \frac{T}{1 - I_s/I_{sc}} \quad (39)$$

where $I_{sc} = \alpha m H$ is the instability threshold spin current. Thus, for $0 < I_s < I_{sc}$, the spin current I_s increases the fictitious temperature of the macrospin, whereas for $I_s < 0$, it decreases the fictitious temperature. The threshold I_{sc} corresponds to a singular point in \tilde{T} , consistent with instability. This fictitious temperature concept, while relatively crude and strictly applies only to a macrospin system in a simple external magnetic-field-induced potential, is nevertheless instructive. It describes the change of the thermally distributed states of the macrospin upon the introduction of a spin torque. It also gives some conceptual guidance to the process of spin-torque-induced excitations in a thin-film geometry involving magnetic inhomogeneity such as domain walls.

A more mathematically rigorous treatment of the finite-temperature macrospin dynamics is to solve the corresponding finite-temperature Fokker–Planck equation.

Fokker–Planck Equation Treatment of Finite-Temperature Spin-Torque Problems

Fokker–Planck equation describes the time-dependent evolution of the ensemble-averaged probability distribution of a system in a given environment and initial condition. For a macrospin, one defines a probability density function $P(\mathbf{n}_m, t) = P(\theta, \varphi, t)$ that is the time-dependent probability of finding the macrospin in the solid angle of $\sin\theta d\theta d\varphi$ with a spherical coordinate set (θ, φ) describing the magnet's direction, \mathbf{n}_m . The Fokker–Planck equation describes the dynamic flow of this probability as a function of space (on the surface of a unit sphere in this case) and time in the form of [68]

$$\frac{\partial P}{\partial t} + \nabla \cdot \mathbf{J} - D\nabla^2 P = 0 \quad (40)$$

where

$$\mathbf{J} = P \frac{d\mathbf{n}_m}{dt} \quad (41)$$

is the ballistic (zero-temperature) part of the probability current and $D\nabla^2 P = \nabla \cdot \mathbf{J}_D$ is the diffusive part of the probability current, with $\mathbf{J}_D = D\nabla P$. The constant D describes diffusion rate in the probability phase space and can be determined via the fluctuation–dissipation relation using equilibrium state comparison with the Boltzmann distribution, which yields $D = \gamma\alpha k_B T/m$. $d\mathbf{n}_m/dt$ is of course just the LLG equation, in this case with a spin-torque term included:

$$\frac{1}{\gamma} \left(\frac{d\mathbf{n}_m}{dt} + \alpha \mathbf{n}_m \times \frac{d\mathbf{n}_m}{dt} \right) = \mathbf{n}_m \times \mathbf{H}_{\text{eff}} + \left(\frac{I_s}{m} \right) \mathbf{n}_m \times (\mathbf{n}_m \times \mathbf{n}_s). \quad (42)$$

Equations 40, 41, and 42 give a set of partial differential equations that can be solved at least numerically, and in some special cases analytically with approximation, to give $P(\theta, \varphi, t)$, which is a statistical description of the evolution of the macrospin in time and position. For detailed discussions on the Fokker–Planck treatment of a macrospin under STT excitation, please refer to references [69–76].

Switching Speed and Dynamics of a Macrospin Under Spin Torque

One area of potential applications of a spin-torque-driven device is in magnetic memories. For such applications it is important to understand the switching behavior of a nanomagnet under the influence of a spin torque, both in its fundamental (zero-temperature) behavior and in its finite-temperature state. While a detailed treatment of this problem even under the macrospin simplification would still

involve the full complexity of the Fokker–Planck equation mentioned earlier, the concept of this can be quantitatively illustrated using a simplified physical picture as illustrated below.

Thermalized Initial Condition

Assume a simple uniaxial anisotropy well with collinear axis to \mathbf{n}_s . Then at an equilibrium initial state, the probability of finding n_m at position (θ, φ) is simply

$$P(\theta, \varphi; t)|_{t=0} = P(\theta) = P_0 \exp\left[-\frac{U(\theta)}{k_B T}\right] \tag{43}$$

with $U(\theta) = (1/2) mH_k \sin^2\theta = E_b \sin^2\theta$, where $E_b = (1/2) mH_k$ is the uniaxial anisotropy barrier height and H_k is the uniaxial anisotropy field. Equation 43 is normalized to $1 = \int_0^\pi P(\theta) \sin\theta d\theta$.

The ensemble average of the moment \mathbf{m} is

$$\langle \mathbf{m} \rangle \approx m(1 - \langle \theta^2 \rangle / 2) \mathbf{e}_z \tag{44}$$

and

$$\langle \theta^2 \rangle = \frac{k_B T}{E_b}. \tag{45}$$

The thermal distribution of states in (θ, φ) space is on a unit sphere surface near the easy-axis direction, as illustrated in Fig. 4 by the red cloud around the north pole.

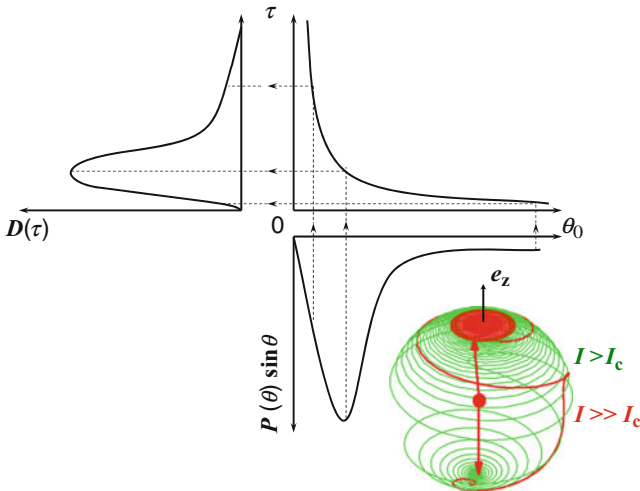


Fig. 4 An illustration of the relationship between an initial angle dependence of switching time $\tau(\theta)$, the thermal initial angle distribution function $P(\theta)$, and the distribution of switching time $D(\tau)$. The curve of τ versus θ_0 is from Eq. 46

Super-Threshold Spin Torque and Switching Speed

First consider the zero-temperature situation where a precessional reversal results when a spin-polarized current I is applied through the nanomagnet at time $t = 0$. Assume a super-threshold condition where I exceeds the intrinsic threshold $I_c = (2e/\hbar) (\alpha/\eta) m (H + H_k)$, where e is electron charge, α the Landau–Lifshitz–Gilbert (LLG) damping constant, and η is the spin polarization of the current as discussed in section “Zero-Temperature Macrospin Dynamics.” The switching time as defined in reference [21] is, for a small initial angle, $\theta = \theta_0 \ll 1$ and a linearized LLG equation for estimating the growth rate of θ from its small initial value to around $\pi/2$ under $I > I_c$ is:

$$\tau \approx \frac{\tau_0}{(I/I_c - 1)} \ln\left(\frac{\pi}{2\theta_0}\right) \quad (46)$$

$$\text{with } \tau_0 = \left(\frac{\hbar}{2\mu_B}\right) \frac{1}{(H+H_k)\alpha} = \frac{(m/\mu_B)}{\eta(I_c/e)}.$$

Equation 46 describes the relationship between the initial angle θ_0 at time $t = 0$, defined as the time when the spin-polarized current incurs a step rise from zero to the value of I and the amount of time τ it takes for the nanomagnet to subsequently reverse its moment under the influence of the spin current and at zero temperature.

To treat finite-temperature effects simply, one first considers an approximation and assumes that the only effect from finite-temperature thermal agitation is on the initial condition distribution $P(\theta)$. In this case, a direct relationship can be established between the initial angle distribution and the switching time distribution function $D(\tau)$, as illustrated in Fig. 4. Note the very large angle behavior of $\tau(\theta)$ would not follow the exact form of Eq. 46 which is only a small θ expansion form. The conceptual relationship however remains valid, and for most practical situations, the approximation Eq. 46 remains useful, as large initial angle events are truncated by the exponentially decreasing probability in $P(\theta)$. Also, the time the trajectory spent in large θ territory after a large $I > I_c$ excitation is relatively short compared with the time it takes for the initial growth of θ [21].

The thermal-fluctuation-dictated initial angle is random in φ . The average angle for θ for a nanomagnet containing only an uniaxial anisotropy is:

$$\langle \theta \rangle \approx \frac{\int_0^\infty \exp(-\xi\theta^2) \theta \sin \theta d\theta}{\int_0^\infty \exp(-\xi\theta^2) \sin \theta d\theta} \approx \sqrt{\frac{\pi}{4\xi}} \quad (47)$$

with $\xi = E_b/k_B T$. The corresponding reversal time average over the results of Eq. 46 with θ set to be thermal initial value of $\langle \theta \rangle$ is:

$$\langle \tau \rangle \approx \frac{1}{2} \ln\left(\frac{\pi}{2}\right) \tau_I (\ln \xi + C) \quad (48)$$

where $C = -\int_0^\infty \exp(-\gamma) (\ln \gamma) d\gamma = 0.57722$ is the Euler number and

$$\tau_I = \tau_0 / (I/I_c - 1). \quad (49)$$

One may also compute the distribution function $D(\tau)$ defined on $\tau \in [0, +\infty]$ as $D(\tau) d\tau = P(\theta) \sin \theta d\theta$. This gives

$$D(\tau) = \frac{\pi^2}{2\tau_I} \xi \exp \left[-\left(\frac{\pi}{2}\right)^2 \xi \exp \left(-\frac{2\tau}{\tau_I} \right) - \frac{2\tau}{\tau_I} \right] \quad (50)$$

which has a peak position at

$$\tau_{pk} = \left(\frac{\tau_I}{2}\right) \ln \left(\frac{\pi^2 \xi}{4}\right). \quad (51)$$

and the peak value

$$D(\tau_{pk}) = \left(\frac{2}{e}\right) \left(\frac{1}{\tau_I}\right). \quad (52)$$

Beyond the peak, $D(\tau)$ decays with a time constant of $\tau_I/2$. Thus the width of $D(\tau)$ is $\Delta\tau = \tau_I/2$ and is only weakly dependent on ξ .

The probability of the junction having not switched at time t is defined as

$$E_r(t) = 1 - \int_0^t D(\tau) d\tau = 1 - \exp \left(-\frac{\pi^2 \xi}{4} e^{-\frac{2t}{\tau_I}} \right) + O \left[\exp \left(-\frac{\pi^2 \xi}{4} \right) \right] \quad (53)$$

which in the limit of $t/\tau_I \gg 1$ leads to the residual error's asymptotic relation

$$E_r(t) \approx \left(\frac{\pi^2 \xi}{4}\right) \exp \left(-\frac{2t}{\tau_I} \right) + O \left[\exp \left(-\frac{\pi^2 \xi}{4} \right) \right], (E_r \ll 1). \quad (54)$$

This residual error function is robust against a small adiabatically administered initial tilt of the easy axis. The initial tilt angle θ_i would modify $E_r(t)$ only in terms of the order $\exp(-\pi^2 \xi/4)$ or smaller.

A treatment of the problem using the Fokker-Planck formulation [68, 69] includes additional thermal effects such as the diffusion of initial states over time and the diffusive nature of probability evolution during reversal. This gives rise to a very similar result, with the same time-dependence component and an amplitude prefactor that appears to be within a factor of 2 of that for Eq. 54.

Equation 54 can be equivalently viewed as a probability distribution function for the switching threshold current I if one fixes the switching time t at a certain switching pulse width in time and explicitly writes out the switching error function

E_r (with an appropriate normalization prefactor) in terms of I by inserting the definition of τ_l from Eq. 49 into Eq. 54. This obviously gives an exponentially decreasing E_r at $I \gg I_c$ limit.

Similar to the situation in time-variable expression, this also points to a small but finite residual probability for the nanomagnet to not switch for any given time at drive current I . This is the nature of STT-induced switching, corresponding to the condition for zero average spin torque per precession cycle which would always be present due to the $\sin \theta$ dependence of the spin torque. In a finite-temperature scenario, this corresponds to a small region for initial state distribution on the (θ, ϕ) unit sphere near the equilibrium position before the spin torque is turned on. States within this region would experience asymptotically zero initial spin torque per cycle of precession, and the switching time would become very long as a consequence. This result is robust within a macrospin model. Experimentally the situation can be more complex due to internal degrees of magnetic freedom as well as a more complex energy potential landscape especially at finite temperature.

Comparison between this simple, initial condition-only model calculation described in the previous sections and a mathematically more rigorous, numerically evaluated full Fokker–Planck equation calculation has also been done [69]. The results of this simple model appear in reasonable agreement, with a full Fokker–Planck result generating slightly faster switching times at the low overdrive ($I/I_c \sim 1$) limit. The exponentially decreasing tail of the non-switching probability E_r , either in τ or in I , remains essentially the same [69, 75, 77]. This tail, however, is yet to be experimentally observed, probably due to the non-macrospin nature of the devices experimentally studied to date [78, 79]. Higher-precision statistics at shorter switching time (well below 10ns) and for smaller junctions (probably below 20 nm) would bring experimental situation closer to the macrospin model assumptions, and one would have a better understanding of whether this macrospin model predicted “stagnation” behavior [69, 75, 77] and is likely to cause practical problems for reliable write operation for a memory element in its small-size limit, for example.

Subthreshold: Spin-Torque-Amplified Thermal Activation

In the limit of $I \ll I_c$ and at finite temperature, there remains a finite probability that the macrospin would be excited over the top of its uniaxial barrier and switch directions. This process is governed by thermal activation assisted by spin torque. The thermal-activated reversal for a macrospin in a uniaxial potential without spin torque was well known [68]. It gives a lifetime before transition of the form $\tau = \tau_A \exp\left[\xi(1 - H/H_k)^2\right]$ with $\tau_A \approx \pi\hbar/\mu_B H_k$ the inverse of the characteristic frequency at the bottom of the uniaxial potential well. Follow the discussion of section “Finite-Temperature Macrospin Dynamics,” a rescaling of the macrospin’s temperature by a fictitious \tilde{T} reflecting the involvement of spin torque that gives explicitly the role of spin torque as

$$\tau = \tau_A \exp \left[\xi (1 - H/H_k)^2 (1 - I/I_c) \right], \quad (55)$$

which gives the probability of the macrospin not switching at the long time limit of $t \gg \tau_A$ after the application of spin torque as approximately

$$E_r(t) = \exp \left[- \left(\frac{t}{\tau_A} \right) \exp \left(- \xi \left(1 - \frac{I}{I_c} \right) \right) \right], \quad (I \ll I_c). \quad (56)$$

These relationships and concepts are important for the discussion of spin-torque-based memory device's switching speed, switching distribution, memory retention, and stability against read disturbance.

A more careful treatment with full Fokker–Planck formalism has been carried out as well [70, 74, 80, 81]. The results are generally similar to Eq. 56, except when in simple uniaxial anisotropy field and in collinear alignments, when one expects an exponent of 2 instead of 1 for the factor $(1 - I/I_c)$ term in Eq. 56 [75, 82]. This exponent of 2 case however is a very special one, requiring the exact knowledge of the shape of the energy potential at the top of the barrier, as well as a precise collinear geometry for magnetic anisotropy, applied field if any, and the spin-polarization directions.

A closer examination mathematically [83] at the apparent exponent β of the $(1 - I/I_c)^\beta$ shows it will depend on the details of the quantitative and specific magnetic configurations. Sample numerical results from the study show such apparent value of β can easily cover the whole range of $1 \leq \beta \leq 2$.

Detailed quantitative experimental comparison remains difficult, as the limit of $I/I_c \ll 1$ is hard to achieve in an MTJ with laboratory time scale in most experiments with sufficiently high-energy barrier E_b . Despite such difficulties, some recent experiments successfully established some quantitative comparison between measurement and model estimates [76, 84, 85], using perpendicularly magnetized spin-valve systems, although the devices experimented with, while relevant to technological applications, remain too large in size to be directly compared to the simple analytical results of macrospin models.

Exchange Stiffness, Internal Degrees of Freedoms, and Magnons

For a thin-film magnet under spin torque, as discussed in section “[Time Scales, Length Scales, and Constitutive Relationship for Spin-Torque Dynamics in Continuous Medium](#),” the internal degrees of freedoms would significantly affect the thin-film response. Those problems are generally highly complex and can only be solved using numerical integration of the LLG equation over the volumes involved. Several conceptual issues, however, may be worth more discussion.

Linearized LLG in the Continuous Medium Limit Containing a Spin-Torque Term

In this limit, one assumes the magnetic thin film is near its equilibrium easy-axis direction. For simplicity further assume the easy axis is collinear with the spin polarization of the reference layer direction and that of the applied magnetic field if any, further simplifying Eq. 29 to ignore any spatial dependence of spin torque τ_{ij} . Following the treatment of spin waves within LLG by, for example, Herring and Kittel [43], after some algebra one arrives at a linearized instability threshold for spin torque to destabilize any particular spin-wave mode with momentum vector $\mathbf{k} \perp \mathbf{m}$ as

$$I_c(k) = \left(\frac{2e}{\hbar}\right) \left(\frac{\alpha}{\eta}\right) m \left(H_k + H + \frac{Dk^2}{2\mu_B}\right) \quad (57)$$

with the effective spin polarization η assuming the same forms as discussed in section “Zero-Temperature Macrospin Dynamics” for spin valves and MTJs, respectively. Here D is the spin-stiffness constant often used to parameterize the long-wavelength spin-wave (magnon) dispersion characteristics in the form of magnon energy $\varepsilon(k) = Dk^2$. For Co, for example, $D \approx 0.5 \text{ eV}\text{\AA}^2$ [62].

Note that Eq. 57 is for one specific spin-wave mode with a unique \mathbf{k} . This is often nonphysical I_c , in the sense that there could be other instabilities in lower k modes (e.g., macrospin being $k = 0$ is the lowest). Any excitation of such lower-lying modes would cause a growth of excitation amplitude, breaking the small-angle linearized LLG equation assumption. In certain boundary conditions, however, it is possible to shift the stability thresholds of these different modes differently, and a finite k mode could become the lowest-lying threshold. One conceptual example would be a circular nanomagnet thin film with circumferential edge magnetic moments completely pinned in one direction. In such a case the threshold for $k = 0$ macrospin would become very high due to exchange energy cost compared to a finite k mode with the wavelength corresponding to the size of the nanomagnet.

Confined Spin-Current Excitation of Spin Waves, One Quantitative Example

One boundary condition problem related to spin-wave excitation by spin torque is solved within the linearized LLG framework by Slonczewski [49]. This is a model system with a radius a circular confinement of spin-current injection area and an extended magnetic thin film for outward-radiating spin waves. The magnetic film’s easy axis and the applied field are perpendicular to the film direction. For such a boundary condition, the threshold current is calculated to be

$$I_c = \left(\frac{2e}{\hbar}\right) \left(\frac{6.31}{2\pi}\right) \left(\frac{\alpha}{\eta}\right) m \left[H_{\text{eff}} + \left(\frac{0.7515}{\alpha}\right) \frac{D(\pi/2a)^2}{2\mu_B} \right]. \quad (58)$$

The intercept of this threshold expression at zero H_{eff} reveals a rather intrinsic threshold for initiating magnon excitation and propagation that is independent of contact size a :

$$I_{cw} = 5.85 \left(\frac{2e}{\hbar} \right) \left(\frac{M_{st}}{\eta} \right) \left(\frac{D}{2\mu_B} \right) \quad (59)$$

which for 1 nm thick Co type of films with $D \approx 0.5 \text{ eV}\text{\AA}^2$ at $\eta = 0.5$ gives an $I_{cw} \approx 1.5 \text{ mA}$.

Experiments

Exploration of interaction between ferromagnetic bodies and charge-current-carrying spin current began in the 1970s and 1980s [8, 16, 17, 86–88]. The pace of experimental work accelerated significantly in the last decade, originating from several factors including a clearer theoretical understanding, as well as a more direct access to controlled experiments and device structures allowing quantitative investigations, thanks to the development of modern fabrication technologies. Potential applications in solid-state electronics further fuel the interest and accelerate the progress.

Spin-Torque-Induced Magnetic Excitation and Switching

Early experiments that directly reflect the action of spin torque were done using giant magnetoresistance (GMR)-based metallic multilayers with point contact [22, 23], in nearly half-metallic manganite ferromagnetic junction structures [20, 24] and in electron-beam lithographically patterned Co/Cu/Co nanostructured spin-valve pillars [25]. These experiments demonstrate the presence of a current-induced change in junction resistance. The change has a threshold-like behavior, and the threshold shows systematic dependence on applied magnetic field. A few of the experiments went on to demonstrate full bias-current-induced hysteretic magnetic reversal of one of the layers constituting the device structure [20, 24, 25]. The observed threshold switching current demonstrated the expected dependence on applied magnetic field [20, 24, 25], suggesting the presence of a spin-torque-induced switching mechanism. Further proof for the involvement of spin-torque-driven dynamics was shown when continuous microwave oscillation was observed in nanomagnet pillar-based spin-valve junctions [89]. There has since been a large body of both experimental and theoretical works exploring the nonlinear oscillator behavior of a nanomagnet under the influence of a spin-torque term. For in-depth discussions, the readers are referred to Refs. [90–93] and references therein.

The effect of spin torque on finite-temperature thermal-fluctuation process was recognized when experiments with nano-patterned CPP spin valves revealed a finite

subthreshold switching probability whose resulting probabilistic switching rate as a function of the drive current amplitude showed a log-linear dependence, characteristic of thermal activation [94, 95]. These experimental works led to the quantitative description of the finite-temperature spin-torque dynamics described in section “[Finite-Temperature Macrospin Dynamics](#).”

The general behavior of the experimentally observable spin-torque switching threshold value and its statistical properties over different time scales has been well studied both for spin-valve systems and for tunnel junction-based nanomagnets. Detailed quantitative understanding however has been complicated by two factors – the often complex magnetic anisotropy energy potential involving orthogonal easy-axis and easy-plane anisotropies and non-macrospin-related magnetodynamics. The first factor makes it difficult to have accurate analytical expressions for the description of the switching probability as it depends on the amplitude and time duration of the spin torque even in the very simple macrospin model. The second factor makes macrospin model inaccurate for device sizes much larger than around 20 nm for quantitative work. Both issues are being addressed, thanks to materials and lithography technology improvement. A new generation of spin-torque switches has emerged, based on magnetic films having net perpendicular anisotropy (PMA films) [85, 96–99], which makes the modeling more accurate as analytical results can be obtained in many cases. Direct comparison with experiment reveals valuable insight into the roles different materials parameters play [76, 78, 85, 100]. Advances of lithography tools and technologies have at the same time enabled fabrication of device structures below 20 nm in size, making it feasible to realize a nearly macrospin-like experimental system, facilitating quantitative comparison with theoretical understanding [78, 101–103].

Spin Torque in Magnetic Tunnel Junctions

After the observation of spin torque in early magnetic nanostructures mostly based on all-metal spin valves or magnetic oxides, a significant experimental advance was the observation of spin-torque effects in magnetic tunnel junctions. The first observation was reported in permalloy– AlO_x –permalloy tunnel junctions [38]. The presence of spin-torque-induced switching in tunnel junctions means it is now possible to impedance match a spin-torque switchable device with that of VLSI CMOS technology, thus opening up possibilities for CMOS-integrated applications. The advance of MgO-based very high MR MTJ further made these applications feasible, as it was soon clear that MgO-based magnetic tunnel junction can also be switched by spin torque and with greater effectiveness [104, 105]. These experiments also brought forth a major materials advance by making use of the CoFeB as precursor materials for the tunnel electrodes in combination with MgO (100) tunnel barrier. The method of thin-film stack synthesis utilizes high-precision sputter deposition tools together with an optimized postdeposition anneal route for

ensuring the proper orientation alignment between the MgO (100) tunnel barrier and the resulting (bcc) crystalline CoFeB tunnel electrodes for large MR [106].

The high-quality MgO-based tunnel junction made available during this period also enabled quantitative measurement, for the first time, of the magnitude and bias voltage dependence of the spin torque in such devices [47]. These measurements confirmed the theoretical understanding of a nearly linear dependence between the “in-plane” component of the spin torque τ_{\parallel} and tunnel junction bias voltage at low bias (below 0.4 V), as discussed in sections “[Magnetic Tunnel Junction and a Tunnel Barrier Interface for Spin Transport](#)” and “[Zero-Temperature Macrospin Dynamics](#).” It also revealed the presence of a significant “perpendicular” torque τ_{\perp} that is quadratically bias dependent, consistent with earlier studies of an exchange-like interaction across a tunnel barrier [8, 107–109]. More recently, these measurements have been extended to higher tunnel junction voltages by employing a low-duty-cycle time-resolved resonance technique, where a nonlinear apparent reduction of τ_{\parallel} against bias voltage above 0.4 V was seen in one polarity [110].

Applications

Spin torque provides an effective way of manipulating nanometer-sized ferromagnets using a spin-polarized current. This has been recognized early on as possibly enabling a magnetism-based all-solid-state memory. Such memory, usually called magnetic random-access memory or MRAM, has been in development for years for special niche applications that require fast, nonvolatile, and radiation-hard memories. First-generation MRAMs use current-induced magnetic field for writing of magnetic bits, which suffer from increasing demands of the amount of magnetic field required for writing as the bit size is scaled down. The technology is generally viewed as unsuitable for magnetic bit sizes much below 100 nm because of the extraordinary amount of write current that does not scale with semiconductor technology. Spin torque provides an effective alternative means of writing a small magnetic bit using spin-polarized current that can be scaled down to smaller sizes – perhaps to ten nanometers or below – before eventually reaching the tunnel barrier’s maximum allowed current density.

Spin-torque-induced magnetic oscillations occur at microwave frequencies and have been explored for applications where a compact and tunable microwave source is desirable such as for short-distance communications between circuits. Spin torque is also a force present during the operation of a magnetic-field sensor based on MTJ or spin valve, such as the types used in magnetic hard-disk readers. There the noise and dynamics characteristics are affected by spin torque. More recent discussions have broadened to the possible use of a spin-current controllable magnetic device as a logic-gate element that may offer some advantages over CMOS for certain applications at advanced technology nodes in terms of power dissipation and nonvolatility of intermediate logic states [111, 112].

Spin-Torque Switchable Magnetic Tunnel Junction as Memory Devices

Idealized Device Characteristics

A two-terminal junction having two or more stable states that can be switched using a controlled amount of bias current (or voltage) constitutes a memory element. To make effective use of such an element in advanced CMOS circuit environment requires the two-terminal device's electrical impedance and signal swing to match that of the CMOS transistor-based circuits. This was enabled by the discovery of MgO-based MTJs with large MR well over 100 %. The simplest circuit element for such memory application has current–voltage characteristics as shown in Fig. 5a.

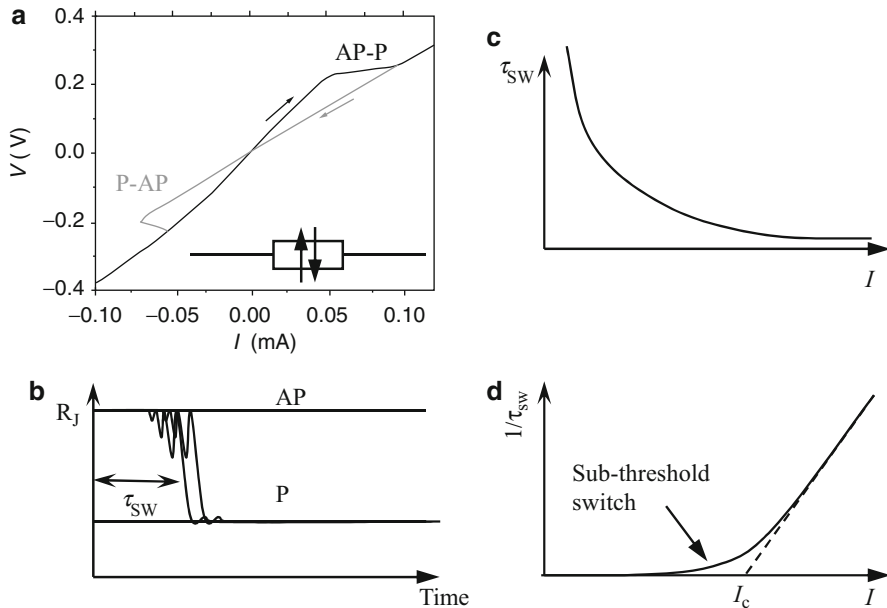


Fig. 5 The basic device characteristics of a spin-torque-based two-terminal switching element, in the macrospin limit. (a) The I–V characteristics under nearly constant voltage drive showing the low-resistance (magnetically parallel or P) state and the high-resistance (magnetically antiparallel or AP) state and the switching thresholds between the two states. *Inset*: a possible symbol for the spin-torque-switched MTJ as a two-terminal circuit element. (b) The time–domain behavior of the junction resistance during switching. Thermal noise would cause the exact switching time τ_{sw} to fluctuate with a well-defined probability distribution that is described in section “Switching Speed and Dynamics of a Macrospin Under Spin Torque.” The oscillation in this illustration is only meant to show magnetic precession. Its resistance change may be minimal especially if the MTJ is of the type involving only symmetric, perpendicularly magnetized films whose magnetic precession around easy axis would not result in resistance oscillation. (c) The relationship between switching time τ_{sw} and the drive current (or voltage) amplitude when driven above the threshold I_c or V_c , as defined by Eq. 46. (d) The dependence of mean switching speed $1/\tau_{sw}$ on bias amplitude. Above threshold the linear dependence and its distribution are governed by Eqs. 46 and 53. Below the threshold, by Eqs. 55 and 56

The threshold voltage for an MTJ can be estimated using Eq. 34, which relates switching threshold voltage V_c or the corresponding P-AP threshold current $I_c = G_p V_c$ to the uniaxial anisotropy barrier height $E_b = mH_k/2$ when considered within the macrospin model assumptions, giving

$$I_c = \left(\frac{4e}{\hbar}\right) \left(\frac{\alpha}{\tilde{\eta}}\right) E_b \quad (60)$$

where $\tilde{\eta}$ is defined by Eq. 35. For macrospin, typical materials parameters would indicate an I_c of the order of 30–50 μA if $E_b \approx 60k_B T$ where $T = 300$ K. Of experimentally verified devices with sizes larger than 30 nm or so, the I_c tend to be significantly larger than such macrospin-derived values. This is believed to be related to non-macrospin behavior of finite-size devices and in particular a form of thermal and spin-torque excitation that is sub-volumes [78, 102, 103].

Equation 60 indicates a minimum write current independent of junction size if one is to maintain the same data retention lifetime or E_b . This is likely the ultimate limiting factor for scaling of spin-torque-based MRAM bit size [20, 21, 113]. Given a tunnel barrier's current density threshold for damage to be of the order 10^7 A/cm^2 , one should expect the junction size to be scalable down to about 10–20 nm, while if using all-metal spin-valve type of structures, either directly or via the nonlocal spin-current approach discussed below, the limiting current density is likely to be an order magnitude or so higher, and hence the magnetic bit size another factor of 3–10 down, or to perhaps around 5 nm, and limited not so much by write-related breakdown as by the achievable E_b in such small volumes.

Above threshold, there is a trade-off between write current and write speed. The product of write current I_w and write time τ_w follows a simple conservation relationship of

$$(I_w - I_c)\tau_w \approx \left(\frac{m}{\mu_B}\right) \left(\frac{e}{\tilde{\eta}}\right) \kappa \quad (61)$$

which is a reflection of angular momentum conservation during the spin-torque switching process. A numerical factor κ describes the details of the write-probability distribution's shape. For a τ_w defined as the peak switching probability density in time, $\kappa = (1/2)$ in $(\pi^2 E_b / 4k_B T)$ according to Eq. 51.

Equation 61 suggests an improvement of switching speed upon the reduction of the total magnetic moment m . Thus switching speed usually improves for smaller junction bits. For a typical junction of the lateral size of somewhere between 50 and 100 nm, $(I_w - I_c)\tau_w \approx (0.1-1) \times 10^{-12}$ Coulomb depending on device size and total magnetic moment involved. This relationship is illustrated in Fig. 5c, d.

Below threshold I_c and at finite temperature, there is a finite probability for thermally activated reversal. This is discussed earlier in section “[Sub-Threshold: Spin-Torque-Amplified Thermal Activation](#).” It relates to memory applications because (a) the thermal activation lifetime Eq. 55 limits the data lifetime of stored data bit, and (b) when reading a data bit, finite bias voltage (and current) is applied,

which can lower the effective activation barrier (e.g., making $E_b \rightarrow E_b (1 - I/I_c)$), shortening data retention time. This is the so-called read-disturb which needs to be taken into account during memory design. Note that this process redistributes the probability function around the energy minimum, and it takes some time for this redistribution to complete [75]. The time scale involved is on the order of τ_A/α [76] where $\tau_A \approx \pi\hbar/\mu_B H_k$ is the magnetic attempt frequency-related time scale and α the LLG damping. Nonlinear mode coupling among different magnons may affect this time scale too.

Spin-Torque Switching Efficiency and Control of Magnetic Anisotropies

A key attribute to improve for CMOS-integrated memory application is the amount of current needed for spin-torque-induced magnetic switching. It needs to be minimized while at the same time retaining the devices' ability to store information for extended periods of time (typically 10 years as a specification). That is, one needs to minimize I_c while maintaining a certain value of E_b .

A thin-film MTJ's magnetic anisotropy can have a variety of forms. The situation that is theoretically easiest to analyze involves a single uniaxial anisotropy, in which case the threshold current is directly proportional to the barrier height, as discussed in sections “Zero-Temperature Macrospin Dynamics” and “Idealized Device Characteristics.” This is not naturally the case for a thin-film-based MTJ whose free layer tends to experience strong shape-induced demagnetization field keeping the moment in-plane. In fact, the earlier demonstrations of spin-torque switching devices were all made using devices with predominantly in-plane magnetic anisotropy (IMA for short) thin films. In such cases, the uniaxial anisotropy axis is also in-plane and often controlled, at least in part, by a high-aspect-ratio (e.g., 1:2–1:4) shape of the MTJ. In such configurations, in addition to the uniaxial anisotropy, there is a strong easy-plane anisotropy $4\pi M_s$, which results in a much increased spin-torque switching threshold current determined by $m (H_k + 2\pi M_s)$ as discussed at the end of section “Zero-Temperature Macrospin Dynamics.” The easy-plane anisotropy does not contribute to thermal activation barrier height $E_b = (1/2) mH_k$. It therefore dilutes the effectiveness of spin torque, increasing its threshold without correspondingly increasing the desired barrier height.

An obvious remedy for this situation is to make use of thin-film materials with strong crystalline or interfacial anisotropy that is perpendicular to the film surface with a magnitude exceeding that of the in-plane demagnetization energy $2\pi M_s^2$. For such films, the magnetic easy axis would be perpendicular to the film surface. This is the so-called perpendicular anisotropy (or PMA) geometry. These avoid the orthogonal anisotropy-axis configuration of an IMA device, improving switching efficiency.

A common figure of merit to measure the effectiveness of a spin-torque device is the efficiency ratio of E_b/I_{c0} , where I_{c0} represents the zero-temperature instability threshold. In theory at least, within macrospin model assumptions, PMA devices would allow a much better efficiency ratio than IMA devices. This however becomes more complex in reality for devices with sizes much larger than the magnetic layer's exchange length, as the spin-torque switching process becomes

sub-volume and non-macrospin. A non-macrospin junction tends to degrade this efficiency ratio [78, 102]. Generally speaking, junctions with smaller lateral size in comparison with the magnetic exchange length would have better spin-torque efficiency ratio E_b/I_{c0} . This has recently been experimentally observed in sub-50 nm spin-torque switchable MTJs [78, 98, 101–103].

The advantage of PMA-based devices for spin-torque switching was recognized early on, although experimental demonstration required the development of new materials systems and integration of such materials into sub-100 nm lithography environment. It wasn't until 2006 did one see first unambiguous experimental demonstration of spin-torque switching of a PMA material [114] and a (CoNi and CoPd)-based spin-torque switching with improved spin-torque efficiency [115]. These discoveries were rapidly followed up by other PMA materials for switching device exploration since.

Factors Important for Memory Applications

Key to applications of spin-torque-driven MTJ in memories is the availability of an appropriate magnetic thin films with PMA that is compatible with high MR MTJ requirements, such as those using (001) MgO as tunnel barrier. For this the PMA thin films need to have sufficient perpendicular anisotropy to overcome the demagnetization and supply for sufficient uniaxial anisotropy with $E_b > 50k_B T$ or so with T being ambient temperature. The film needs to have as strong an exchange stiffness as possible, so as to make exchange length long enough to be comparable to lateral device dimension to minimize sub-volume agitation-related device property degradation. The film further needs to be highly crystallized, at least at its interface with MgO, with a (bcc) symmetry matched into the (001) orientation of the MgO barrier. This is to satisfy the spin-dependent tunnel junction's requirement for band matching in order to have high spin polarization and large TMR. For technology integration and cost reduction, the tunnel junction materials stack would further need to be compatible with standard CMOS back-end processing temperature, usually around 350–400 C. The combination of these requirements presents a difficult set of challenges for materials development, although amazing progress has been made [79, 97–99, 116] since 2005, when SONY first demonstrated a successful integration of an IMA MgO-based MTJ spin-torque device with a back-end CMOS process [117].

The fundamental scaling of a spin-torque-driven MTJ as a memory element is likely limited by the amount of current density a tunnel barrier can support. To satisfy data retention, an $E_b > 60k_B T$ would usually be necessary, meaning the total current of a switching device is likely to stay above what is dictated by Eq. 60 for a macrospin, which is of the order of 30–50 μA . Assuming a tunnel barrier breakdown voltage of about 0.5 V at an RA product of about 1 $\Omega \mu m^2$, the breakdown current density would be about 5×10^7 A/cm², corresponding to a minimum junction size of about 10 nm across. There are a few additional factors that could mitigate this limit to some degree, such as the Joule heating and hot-electron-induced magnetic heating of the MTJ structure during switching current

application. The macrospin-based value would nevertheless be a good starting point for estimating the device performance one could expect.

The switching or “write” error probability for write pulse width τ and height V decreases with increasing magnitude of the write voltage bias. In macrospin limit and for short pulse width $\tau \sim \tau_0$, the relationship follows Eq. 54, which can be rewritten to read

$$E_r(V, \tau) \approx \left(\frac{\pi^2 \xi}{4} \right) \exp \left[-\frac{2\tau}{\tau_0} \left(\frac{V}{V_{c0}} - 1 \right) \right], \quad \text{for } V > V_{c0} \quad (62)$$

with $\tau_0 = \frac{m/\mu_B}{\eta V_{c0}/R_p e}$ as defined in section “Switching Speed and Dynamics of a Macrospin Under Spin Torque” and $\tilde{\eta}$ as defined by Eq. 35. $\xi = E_b/k_B T$. Experimentally, the observed write error probability *versus* write voltage in 100 nm size devices at $\tau \sim 10$ ns (which doesn’t exactly satisfy the short time limit but close) shows slightly faster decrease [79] than the exponential dependence predicted by Eq. 62, although the observed V_{c0} tend to be a factor of 2–5 larger than macrospin prediction. This is most likely due to the non-macrospin nature of the switching process in combination with the requirement of total angular momentum conservation [78]. The exponential nature of the macrospin switching probability versus write voltage is potentially a concern for devices at scaling limit (when approaching macrospin behavior), as it might limit the achievable write error for a reasonable write voltage. The real device behavior is only just beginning to be experimentally investigated quantitatively. Other high-energy processes may affect the details of switching statistics – processes such as spin–flip scattering of tunnel electrons may cause generation of very short wavelength magnon populations that mimic a non-macrospin situation even when the junction sizes approach macrospin cross-over length scale as estimated by the spin wave’s long-wavelength exchange stiffness.

Nonlocal Spin-Current and Three-Terminal Spin-Torque Devices

As discussed earlier, the transport of spin current, and therefore the presence of spin torque $\tau_{||}$, does not always accompany a charge current. This can be developed further into device concepts, where the charge and spin-current paths are separate, so that various desirable device characteristics, such as read and write impedance, magnetoresistance, and breakdown characteristics, can be optimized separately. Earlier experiments have successfully demonstrated the presence of a pure spin-current-induced voltage signal similar to what was described by μ_s in Eq. 17 [5, 58]. This has led to a pure spin-current-driven magnetic switching without the charge current directly passing the nanomagnet being switched by the spin current [59, 60, 118]. A 3-terminal spin-torque-driven magnetic switch device is experimentally constructed based on these principles [119]. The basic structure is illustrated in Fig. 6. In this structure the injection layer (IL) is magnetic and extended in

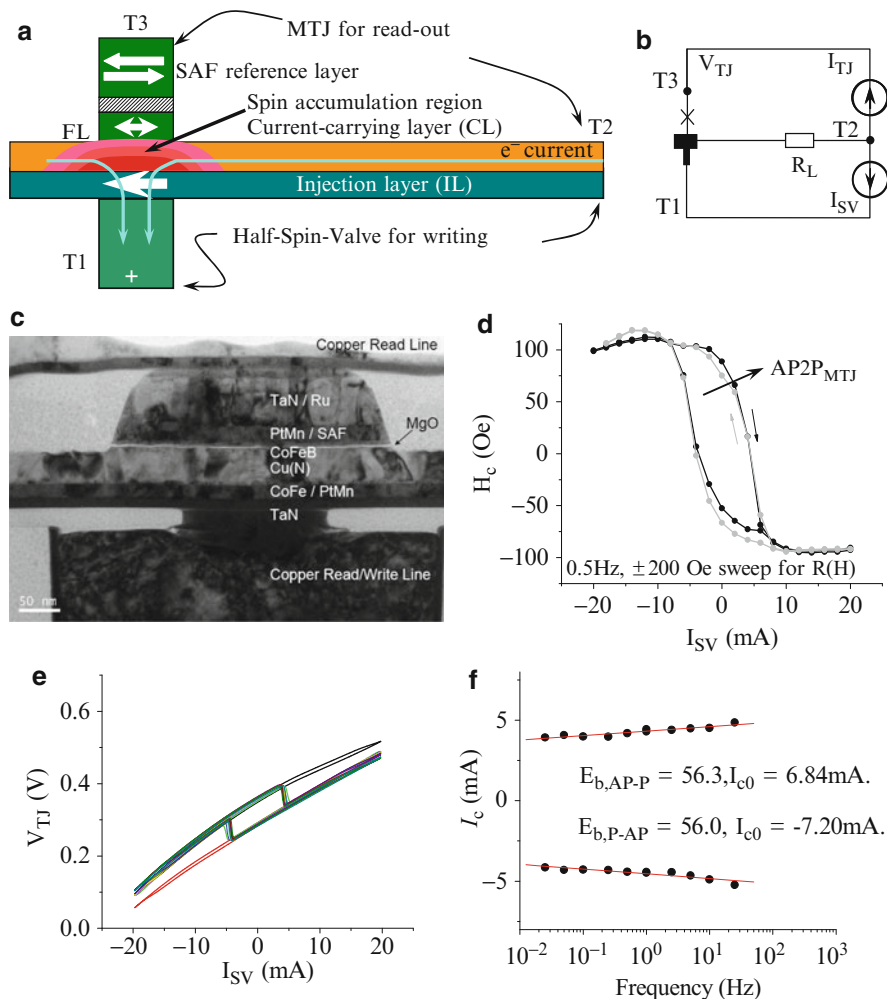


Fig. 6 An illustration of the device structure for a nonlocal spin-current-driven magnetic switch (a). (b) The equivalent circuit of the device. (c) A cross-section transmission electron microscopy image of a device showing the layer compositions. (d) The spin-torque switching phase boundary in (H, I) space. (e) Trans-resistance of the device at different sweep rates of the spin-valve side bias current, from 0.025 to 25 Hz. (f) Sweep-rate-dependent threshold current and the resulting estimate of thermal activation barrier height (d and f, Reprinted with permission from [119, 120, 138], Copyright [2009, 2010], AIP Publishing LLC)

lateral dimensions, and the FL and the synthetic antiferromagnetic (SAF) reference layer are magnetic and patterned down to small sizes. The layer (yellow) between IL and FL is for drawing charge current, as well as coupling spin current to the FL. It is high in electrical conductance and low in spin-flip scattering rate.

The metal structure forming T1 is also patterned down to a size similar to that of the FL to provide the necessary current concentration for spin filtering through IL into the conduction layer. The charge current is injected through terminal T1 and collected at T2. Spin accumulation results in the nonmagnetic layer between T1 and the free-layer (FL) magnet. This spin accumulation drives a spin current that is absorbed by the FL. The spin current thus exerts a spin torque $\tau_{||}$ that can switch the magnetization of the FL. Above the free layer, a magnetic tunnel junction can be built whose resistance state can be read out between terminals T3 and T2. The shared lead resistance between input and output sides from the current carrying layer is shown as R_L in the equivalent circuit (b). A common current path from the read and write circuits traverses the thin-film metal of the current carrying layer, labeled as a resistor of value R_1 in the equivalent circuit in Fig. 6b. The advantage of this device structure is it allows in situ preparation of two interfaces critical for spin transport – that between the injection layer IL and the high-conductance metal layer and that between the high-conductance metal layer and the free layer – thus achieving best spin-transport characteristics. The device has been demonstrated to show switching characteristics similar to those built based on all-metal spin-valve structures for its write characteristics, reaching a threshold current of about 7 mA for Ins switching for a simple in-plane magnetic anisotropy system of CoFeB/Cu for an $E_b \approx 39k_B T$ [119, 120]. For CMOS-integrated applications, further optimization would be necessary. Materials designs utilizing perpendicularly magnetized thin films would improve its spin-torque switching efficiency and reduce the switching current, for example.

There are other 3-terminal devices demonstrated for the separation of read and write current. Some does not depend on the type of nonlocal spin transport discussed above. As shown in Fig. 7, one type of 3-terminal spin-torque switchable device uses a split contact arrangement for the magnetic free layer, thus enabling a direct, spin-valve-like action on the write operation while using a tunnel junction interface for readout [121]. Spin-torque-induced magnetic switching is demonstrated with this device configuration at $70 \times 200 \text{ nm}^2$ size with a 40 nm trench. The fabrication of the trench structure between the contacts above FL is lithographically challenging. A similar device structure but with magnetically coupled while electrically isolated input–output has also been proposed for possible digital logic applications [112].

More recently it has been demonstrated that one could generate the nonlocal spin current required to switch a nanomagnet using spin-Hall effect through spin–orbit interaction [122]. This results in a similar device construct as those shown in [119] but with simpler layout. It has been experimentally demonstrated as an effective way of generating large amount of spin current for switching the nanomagnet. For device applications so far the spin-Hall-based nonlocal spin-current generation seems to be fundamentally confined to a geometry where the spin polarization lies in the plane of the interface the spin current has to cross to enter the nanomagnet [122], making its application somewhat difficult for full PMA structures.

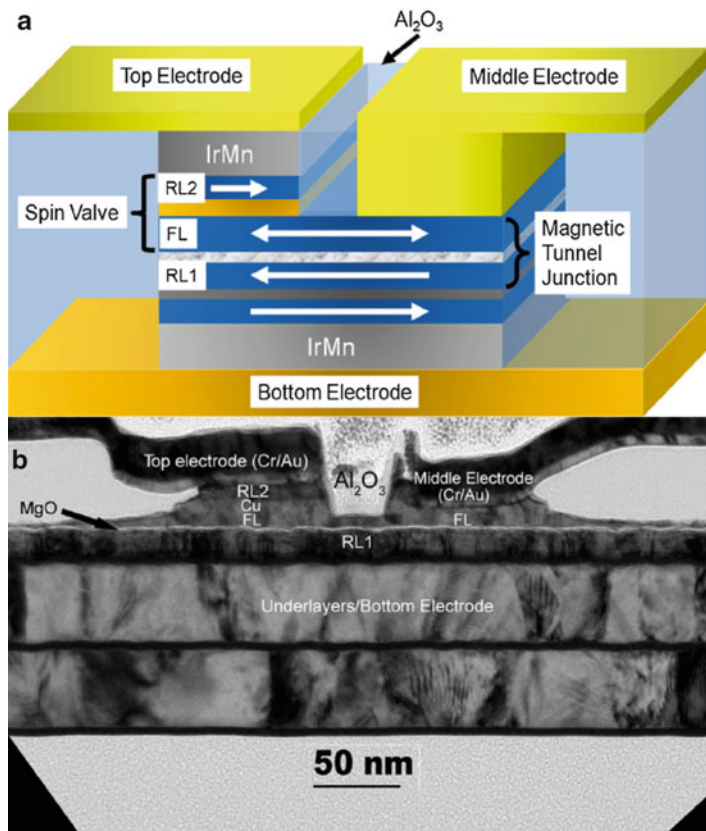


Fig. 7 A 3-terminal spin-torque switchable device using a split contact for the magnetic free layer (© [2009] IEEE. Reprinted, with permission, from [121]). (a) Schematic of the device and (b) a cross-section transmission microscopy picture of the built structure

Open Questions and Future Challenges for Spin-Torque Science and Technologies

After over a decade of intense investigation, the basic phenomena involving spin-torque-related magnetic excitation are reasonably well understood. Promising device applications such as spin-torque-based magnetic random-access memory are well under way. There are however still areas where quantitative scientific understandings lack, and other areas entirely new concept are being proposed and investigated as this article is being written. As a part of the larger inquiry into spin-dependent transport physics in condensed matter, spin-torque physics remains one of the cutting edge studies into the novel properties of matter, with the promise of many potential applications.

So far discussions of spin-torque-related transport and dynamics are mostly limited to semiclassical scenarios, where the ferromagnet is treated essentially as a classical object in terms of its dynamics. The quantum mechanical equivalent of such dynamics is still being developed conceptually [123], which should provide a path for the transition between a semiclassical macrospin picture and that of truly atom-like objects with few spins, including extreme examples, such as the Kondo scattering problem. In such cases the separation of time and energy scales between the ferromagnetic body and the spin-carrying transport carriers may blur or no longer exist, and new insights into relationships between known phenomena may be gained, as well as possible discoveries of new behaviors.

The noise characteristics of spin-torque-related systems are another area of potential interest, both for practical purposes in terms of sensor characteristics and for conceptual understanding. Spin torque couples the noise dynamics between the carrier electrons and that of the ferromagnets involved. A quantitative description of the fluctuation characteristics of such coupled systems far from equilibrium (under the influence of transport current) remains to be established.

There remains a tremendous amount of complexity in spin-torque-related behavior in non-macrospin magnetic systems, as dictated by the nonlinear nature of most spin-torque-related large amplitude excitations. These processes and their relationship to other magnon excitations such as those induced by high-energy tunnel electrons have only recently started to attract attention for quantitative investigations [124].

Recent research begins to investigate spin current related to processes other than tunneling or spin valves. Spin-orbit-related spin-current generation and propagation received much attention [125, 126], including the so-called spin-Hall effect as a source of spin current [127–129]. Direct observation of spin-torque effect using spin current generated by such spin-Hall effect has also recently been demonstrated [129–131], including complete magnetic switching [122]. Discoveries of new state of matter such as topological insulators (see, e.g., Ref. [132, 133] for a review on the subject) might also 1 day lead to new applications.

Spin-dependent transport in a temperature gradient is now being actively studied as well. A full set of spin-transport parameters equivalent to the thermoelectric effects is being established [134, 135]. Experimentally, these in transition metal ferromagnets tend to involve small signal measurements, where separation of thermoelectric and thermal spin-transport phenomena is not always straightforward [136]. Careful studies of the thermodynamic quantities associated with these transport processes also highlighted the often subtle energy-conservation requirement in spin-dependent transport processes in addition to an appropriate treatment of angular momentum and entropy current flow [65].

Spin current is also carried by magnons in ferromagnets. Consequently, a magnon-mediated heat flow is also accompanied by a spin current. A significant amount of spin current may be extracted from thermal gradients involving ferromagnets [137]. With an appropriate combination of materials maximizing heat transport via magnons, these may be turned into useful spin-current devices [137]

with greater efficiency of spin-current generation than the spin-filtering mechanisms based on tunneling or spin valves as discussed in this chapter.

Acknowledgments The author acknowledges valuable and consistent support from IBM Research for his research on this topic.

References

1. Mott NF (1964) *Adv Phys* 13:325
2. Fert A, Campbell IA (1976) *J Phys F* 6:849
3. Valet T, Fert A (1993) *Phys Rev B* 48:7099
4. Son PCV, Kempen HV, Wyder P (1987) *Phys Rev Lett* 58:2271
5. Johnson M, Silsbee RH (1985) *Phys Rev Lett* 55:1790
6. Julliere M (1975) *Phys Lett A* 54:225
7. Maekawa S, Gäfvert U (1982) *IEEE Trans Magn MAG-18*:707
8. Slonczewski JC (1989) *Phys Rev B* 39:6995
9. Meservey R, Tedrow PM (1993) *Phys Rep* 238:173
10. Spin-flip scattering is included phenomenologically and only in the limit of spin-flip scattering life-time \gg momentum-scattering life-time, so as to preserve the electron spin as a “good” quantum-number for sub-band structures
11. Slonczewski JC (2002) *J Magn Magn Mater* 247:324
12. Slonczewski J (2007) In: Kronmuller H, Parkin S (ed) *Handbook of magnetism and advanced magnetic materials*, vol 5, p 2648
13. Slonczewski JC (2005) *Phys Rev B* 71:024411
14. Slonczewski JC (1996) *J Magn Magn Mat* 159:L1
15. Stiles MD, Zangwill A (2002) *Phys Rev B* 66:014407
16. Berger L (1978) *J Appl Phys* 49:2156
17. Berger L (1984) *J Appl Phys* 55:1954
18. Bazaliy YB, Jones BA, Zhang SC (1998) *Phys Rev B* 57:R3213
19. Berger L (1996) *Phys Rev B* 54:9353
20. Sun JZ (1999) *J Magn Magn Mater* 202:157
21. Sun JZ (2000) *Phys Rev B* 62:570
22. Tsoi M, Jansen AGM, Bass J, Chiang WC, Seck M, Tsoi V, Wyder P (1998) *Phys Rev Lett* 80:4281
23. Myers EB, Ralph DC, Katine JA, Louie RN, Buhman RA (1999) *Science* 285:867
24. Sun JZ (2001) *Physica C* 350:215
25. Katine JA, Albert FJ, Buhman RA, Myers EB, Ralph DC (2000) *Phys Rev Lett* 84:3149
26. Slonczewski JC (1974) Unpublished IBM internal memo
27. Moodera JS, Kinder LR, Wong TM, Meservey R (1995) *Phys Rev Lett* 74:3273
28. Miyazaki T, Tezuka N (1995) *J Magn Magn Mater* 139:L231
29. Kwo J, Wertheim GK, Gurvitch M, Buchanan DNE (1983) *IEEE Trans Magn MAG-19*:795
30. Shoji A, Aoyagi M, Kosaka S, Shinoki F, Hayakawa H (1985) *Appl Phys Lett* 46:1098
31. Wulfhekel W, Klaua M, Ullmann D, Zavaliche F, Kirschner J, Urban R, Monchesky T, Heinrich B (2001) *Appl Phys Lett* 78:509
32. Butler WH, Zhang XG, Schulthess TC, MacLaren JM (2001) *Phys Rev B* 63:054416
33. Mathon J, Umerski A (2001) *Phys Rev B* 63:220403
34. Zhang XG, Butler WH (2004) *Phys Rev B* 70:172407
35. Parkin SSP, Kaiser C, Panchula A, Hughes PM, Samant M, Yang SH (2004) *Nat Mater* 3:862
36. Yuasa S, Nagahama T, Fukushima A, Ando YSK (2004) *Nat Mater* 3:868
37. Ikeda S, Hayakawa J, Ashizawa Y, Lee YM, Miura K, Hasegawa H, Tsunoda M, Matsukura F, Ohno H (2008) *Appl Phys Lett* 93:082508

38. Huai Y, Albert F, Nguyen P, Pakala M, Valet T (2004) *Appl Phys Lett* 84:3118
39. Sun JZ, Ralph DC (2008) *J Magn Magn Mater* 320:1227
40. Slonczewski JC, Sun JZ (2007) *J Magn Magn Mater* 310:169
41. Vaz CAF, Bland JAC, Lauhoff G (2008) *Rep Prog Phys* 71:056501
42. Dennis CL, Borges RP, Buda LD, Ebels U, Gregg JF, Hehn M, Jouguelet E, Ounadjela K, Petej I, Prejbeanu IL, Thornton MJ (2002) *J Phys Condens Matter* 14:R1175
43. Herring C, Kittel C (1951) *Phys Rev* 81:869
44. Shanker R (1980) *Principles of quantum mechanics*. Plenum, New York, p 391
45. Brataas A, Nazarov YV, Bauer GEW (2000) *Phys Rev Lett* 84:2481
46. Tserkovnyak Y, Brataas A, Bauer GEW, Halperin BI (2005) *Rev Mod Phys* 77:1375
47. Sankey JC, Cui YT, Sun JZ, Buhman JCS, Ralph DC (2008) *Nat Phys* 4:67
48. Sharvin YV (1965) *Zh Eksp Teor Fiz* 48:984 (*Sov Phys JETP* 21:655 (1965))
49. Slonczewski JC (1999) *J Magn Magn Mater* 195:L261
50. Bazaliy YB (2007) arXiv:0710.2564v1
51. Tsoi M, Sun JZ, Parkin SSP (2004) *Phys Rev Lett* 93:036602
52. Kim W, Lee TD, Lee KJ (2008) *Appl Phys Lett* 93:232506
53. Waintal X, Myers EB, Brouwer PW, Ralph DC (2000) *Phys Rev B* 62:12317
54. Hernández S, Victora RH (2010) *Appl Phys Lett* 97:062506
55. Bauer GEW, Tserkovnyak Y, Huertas-Hernando D, Brataas A (2003) *Phys Rev B* 67:094421
56. Landauer R (1988) *IBM J Res Develop* 32:307
57. Büttiker M (1988) *IBM J Res Develop* 32:317
58. Jedema FJ, Nijboer MS, Filip AT, van Wees BJ (2003) *Phys Rev B* 67:085319
59. Kimura T, Otani Y, Hamrle J (2006) *Phys Rev Lett* 96:037201
60. Yang T, Kimura T, Otani Y (2008) *Nat Phys* 4:851
61. Lifshitz EM, Pitaevskii LP (1981) *Statistical physics part 2, Chapter 7, Magnetism*. Wheaton, Exeter, p 285
62. Kittel C (1986) Chapter 15, Ferromagnetism and antiferromagnetism. In: *Introduction to Solid State Physics*, 6th edn. Wiley, New York, p 434
63. Tserkovnyak Y, Brataas A, Bauer GEW (2002) *Phys Rev B* 66:224403
64. Heinrich B, Tserkovnyak Y, Woltersdorf G, Brataas A, Urban R, Bauer GEW (2003) *Phys Rev Lett* 90:187601
65. Brataas A, Tserkovnyak Y, Bauer GEW, Kelly PJ (2012) arXiv:1108.0385v3
66. Thomas L, Parkin SSP (2007) In: Kronmüller H, Parkin S (eds) *Handbook of magnetism and advanced magnetic materials*, vol 2, Micromagnetism. Wiley, New York
67. Mancoff FB, Dave RW, Rizzo ND, Eschrich TC, Engel BN, Tehrani S (2003) *Appl Phys Lett* 83:1596
68. Brown WF (1963) *Phys Rev* 130:1677
69. He J, Sun JZ, Zhang S (2007) *J Appl Phys* 101:09A501
70. Apalkov DM, Visscher PB (2005) *Phys Rev B* 72:180405
71. Apalkov DM, Visscher PB (2005) *J Magn Magn Mater* 286:370
72. Visscher PB, Apalkov DM (2005) *J Appl Phys* 97:10C704
73. Visscher PB, Apalkov DM (2006) *J Appl Phys* 99:08G513
74. Visscher PB (2008) *SPIE* 7036:70360B
75. Butler WH, Mewes T, Mewes CKA, Visscher PB, Rippard WH, Russek SE, Heindl R (2012) *IEEE Trans Magn* 48:4684
76. Liu H, Bedau D, Sun JZ, Mangin S, Fullerton EE, Katine JA, Kent AD (2014) *J Magn Magn Mater* 358–359:233
77. Sun JZ (2006) IBM internal memo
78. Sun JZ, Robertazzi RP, Nowak J, Trouilloud PL, Hu G, Abraham DW, Gaidis MC, Brown SL, O'Sullivan EJ, Gallagher WJ, Worledge DC (2011) *Phys Rev B* 84:064413
79. Nowak JJ, Robertazzi RP, Sun JZ, Hu G, Abraham DW, Trouilloud PL, Brown S, Gaidis MC, O'Sullivan EJ, Gallagher WJ, Worledge DC (2011) *IEEE Magn Lett* 2:3000204
80. Li Z, Zhang S (2004) *Phys Rev B* 69:134416

81. Li Z, He J, Zhang S (2005) *Phys Rev B* 72:212411
82. Zhu R, Visscher PB (2008) *J Appl Phys* 103:07A722
83. Pinna D, Kent AD, Stein DL (2013) *Phys Rev B* 88:104405
84. Bedau D, Liu H, Bouzaglou JJ, Kent AD, Sun JZ, Katine J, Fullerton EE, Mangin S (2010) *Appl Phys Lett* 96:022514
85. Bedau D, Liu H, Sun JZ, Katine JA, Fullerton EE, Mangin S, Kent AD (2010) *Appl Phys Lett* 97:262502
86. Berger L (1986) *Phys Rev B* 33:1572
87. Berger L (1988) *J Appl Phys* 63:1663
88. Hung CY, Berger L (1986) *J Appl Phys* 63:4276
89. Kiselev SI, Sankey JC, Krivorotov LN, Emley NC, Schoelkopf RJ, Buhrman RA, Ralph DC (2003) *Nature* 425:380
90. Slavin A, Tiberkevich V (2009) *IEEE Trans Magn* 45:1875
91. Slavin A, Tiberkevich V (2008) In: Demokritov SO (ed) *Spin wave confinement*. World Scientific, Hackensack, p 195
92. Silva TJ, Rippard WH (2008) *J Magn Magn Mater* 320:1260
93. Ralph DC, Stiles MD (2008) *J Magn Magn Mater* 320:1190
94. Koch RH, Katine JA, Sun JZ (2004) *Phys Rev Lett* 92:088302
95. Sun JZ, Kuan TS, Katine JA, Koch RH (2004) *Proc SPIE* 5359:445
96. Nakayama M, Kai T, Shimomura N, Amando M, Kitagawa E, Nagase T, Yoshikawa M, Ikegawa T, Yoda H (2008) *J Appl Phys* 103:07A710
97. Kishi T, Yoda H, Kai T, Nagase T, Kitagawa E, Yoshikawa M, Nishiyama K, Daibou T, Nagamine M, Amano M, Takahasi S, Nakayama M, Shimomura N, Aikawa H, Ikegawa S, Yuasa S, Yakushiji K, Kubota H, Fukushima A, Oogane K, Miyazaki T, Ando K (2008) *IEEE international electron devices meeting (IEDM)*, doi: 10.1109/IEDM.2008.4796680
98. Ikeda S, Miura K, Yamamoto H, Mizunuma K, Gan HD, Endo M, Kanai S, Hayakawa J, Matsukura F, Ohno H (2010) *Nat Mater* 9:721
99. Worledge DC, Hu G, Abraham DW, Sun JZ, Trouilloud PL, Nowak J, Brown S, Gaidis MC, O'Sullivan EJ, Robertazzi RP (2011) *Appl Phys Lett* 98:022501
100. Liu H, Bedau D, Sun JZ, Mangin S, Fullerton EE, Katine JA, Kent AD (2012) *Phys Rev B* 85:220405(R)
101. Gajek M, Nowak JJ, Sun JZ, Trouilloud PL, O'Sullivan EJ, Abraham DW, Gaidis MC, Hu G, Brown S, Zhu Y, Robertazzi RP, Gallagher WJ, Worledge DC (2012) *Appl Phys Lett* 100:132408
102. Sun JZ, Trouilloud PL, Gajek MJ, Nowak J, Robertazzi RP, Hu G, Abraham DW, Gaidis MC, Brown SL, O'Sullivan EJ, Gallagher WJ, Worledge DC (2012) *J Appl Phys* 111:07C711
103. Sun JZ, Brown SL, Chen W, Delenia EA, Gaidis MC, Harms J, Hu G, Jiang X, Kilaru R, Kula W, Lauer G, Liu LQ, Murthy S, Nowak J, O'Sullivan EJ, Parkin SSP, Robertazzi RP, Rice PM, Sandhu G, Topuria T, Worledge DC (2013) *Phys Rev B* 88:104426
104. Kubota H, Fukushima A, Ootani Y, Yuasa S, Ando K, Maehara H, Tsunekawa K, Djayaprawira DD, Watanabe N, Suzuki Y (2005) *J Appl Phys* 44:L1237
105. Hayakawa J, Ikeda S, Lee YM, Sasaki R, Matsukura T, Takahashi H, Ohno H (2005) *J Appl Phys* 44:1267
106. Choi YS, Tsunekawa K, Nagamine Y, Djayaprawira D (2007) *J Appl Phys* 101:013907
107. Faure-Vincent J, Tiusan C, Bellouard C, Popova E, Hehn M, Montaigne F, Schuhl A (2002) *Phys Rev Lett* 89:107206
108. Tiusan C, Sicot M, Faure-Vincent J, Hehn M, Bellouard C, Montaigne F, Andrieu S, Schuhl A (2006) *J Phys Condens Matter* 18:941
109. Popova E, Keller N, Gendron F, Tiusan C, Schuhl A, Lesnik NA (2007) *Appl Phys Lett* 91:112504
110. Wang C, Cui YT, Katine JA, Buhrman RA, Ralph DC (2011) *Nat Phys* 7:496
111. Endoh T, Ohsawa T, Koike H, Hanyu T, Ohno H (2012) *Symposium on VLSI circuits, Honolulu, 13–15 June 2012, Session 10.3*

112. Morris D, Bromberg D, Zhu JGJ, Pileggi L (2012) DAC 2012, San Francisco, 3–7 June 2012, 21.2
113. Devolder T (2011) *Appl Phys Exp* 4:093001
114. Meng H, Wang JP (2006) *Appl Phys Lett* 88:172506
115. Mangin S, Ravelosona D, Katine JA, Carey MJ, Terris BD, Fullerton EE (2006) *Nat Mater* 5:210
116. Worledge DC, Hu G, Trouilloud PL, Abraham DW, Brown SL, Gaidis MC, Nowak J, O'Sullivan EJ, Robertazzi RP, Sun JZ, Gallagher WJ (2010) International electron devices meeting
117. Hosomi M, Yamagishi H, Yamamoto T, Bessho K, Higo Y, Yamane K, Yamada H, Shoji M, Hachino H, Fukumoto C, Nagao H, Kano H (2005) *IEEE IEDM 2005*. IEEE 0-7803-9269-8/05
118. Kimura T, Hamrle J, Otani Y (2005) *Phys Rev B* 72:014461
119. Sun JZ, Gaidis MC, O'Sullivan EJ, Joseph EA, Hu G, Abraham DW, Nowak JJ, Trouilloud PL, Lu Y, Brown SL, Worledge DC, Gallagher WJ (2009) *Appl Phys Lett* 95:083506
120. Gaidis M, Sun J, O'Sullivan E, Hu G, DeBrosse J, Nowak J, Abraham D, Trouilloud P (2010) *SSDM invited paper F7-1*
121. Braganca PM, Katine J, Emley NC, Mauri D, Childress JR, Rice PM, Delenia E, Ralph DC, Buhrman RA (2009) *IEEE Trans Nanotechnol* 8:190
122. Liu L, Pai CF, Li Y, Tseng HW, Ralph DC, Buhrman RA (2012) *Science* 336:555
123. Wang Y, Sham LJ (2012) *Phys Rev B* 85:092403
124. Balashov T, Takacs AF, Dane M, Ernst A, Bruno P, Wulfhekkel W (2008) *Phys Rev B* 78:174404
125. Manchon A, Zhang S (2009) *Phys Rev B* 79:094422
126. Miron IM, Gaudin G, Auffret S, Rodmacq B, Schuhl A, Pizzini S, Vogel J, Gambardella P (2010) *Nat Mater* 9:230
127. Hirsch JE (1999) *Phys Rev Lett* 83:1834
128. Zhang S (2000) *Phys Rev Lett* 85:393
129. Ando K, Takahashi S, Harii K, Sasage K, Ieda J, Maekawa S, Saitoh E (2008) *Phys Rev Lett* 101:036601
130. Kajiwara Y, Harii K, Takahashi S, Ohe J, Uchida K, Uchida M, Mizuguchi M, Umezawa H, Kawai H, Ando K, Takahashi K, Maekawa S, Saitoh E (2010) *Nature* 464:262
131. Liu L, Moriyama T, Ralph DC, Buhrman RA (2011) *Phys Rev Lett* 106:036601
132. Hasan MZ, Kane CL (2010) *Rev Mod Phys* 82:3045
133. Qi XL, Zhang SC (2011) *Rev Mod Phys* 83:1057
134. Hatami M, Bauer GEW (2007) *Phys Rev Lett* 99:066603
135. Hatami M, Bauer GEW, Zhang Q, Kelly PJ (2009) *Phys Rev B* 79:174426
136. Huang SY, Wang WG, Lee SF, Kuo J, Chien CL (2011) *Phys Rev Lett* 107:216604
137. Slonczewski JC (2010) *Phys Rev B* 82:054403
138. Sun JZ (2010) *Am Phys Soc. March Mtg. Paper J37.004*